CO$_2$ capture feasibility by Temperature Swing Adsorption in heavy-duty engines from an energy perspective

Alexander García-Mariaca [a,*], Eva Llera-Sastresa [b], Francisco Moreno [c]

[a] Energy and CO$_2$ Group, Department of Mechanical Engineering, Aragon Institute of Engineering Research (I3A), University of Zaragoza, Zaragoza 50018, Spain
[b] Department of Mechanical Engineering and CIRCE Research Institute, University of Zaragoza, María de Luna s/n, Zaragoza, 50018, Spain
[c] Department of Mechanical Engineering, University of Zaragoza, Zaragoza 50018, Spain

ARTICLE INFO

ABSTRACT

This study made an energy performance analysis and an estimate of the volume and weight of an innovative carbon capture and storage (CCS) system by temperature swing adsorption (TSA) hybridised with an organic Rankine cycle (ORC) working with the waste heat contained in the exhaust gases of a natural gas engine. To achieve this, two varying-sized engines are simulated across the entire rpm range and under partial engine loads. Subsequently, energy simulations are conducted at two CO$_2$ capture rates (CCR) and employing three sorbents (MOF-74-Mg, PPN-6-CH$_2$-DETA and activated carbon) to compare the CCS-ORC performance. Results demonstrate the viability of installing CCS-ORC systems in heavy-duty vehicles since they require less than 6 % of the total volume of the studied vehicles. The engine power penalty induced by the CCS-ORC system varies from 1.9 % with MOF-74-Mg to 23.5 % with activated carbon at 100 % of CCR, leading to a maximum 6.14 % rise in engine fuel consumption. Finally, the maximum CO$_2$ capture process energy consumption is 631 kJ/kgCO$_2$, 9.9 % lower than the literature reported for TSA. Based on these promising results, applying the hybridised system presented in this paper for CO$_2$ capture in sectors that use heavy-duty engines is a strategy to implement.

1. Introduction

Despite the continuous advances in emerging technologies, such as battery vehicles and hydrogen fuel cells, to achieve near-zero CO$_2$ emissions in freight and passenger road transport, these developments remain insufficient due to their short autonomies, overweight and poor chain supply development, among others [1–3]. For these reasons, this sector continues to use internal combustion engines (ICE) for its propulsion. Nevertheless, to reduce its carbon footprint, it has chosen to migrate from diesel to sustainable fuels such as natural gas (NG) [4,5]. Even though NG is not a renewable fuel, it is expected to facilitate the energy transition of this sector towards a sustainable energy system, as was established by the European Commission in 2022 [6].

However, this sector must achieve CO$_2$ emissions close to zero; for this reason, existing technologies such as carbon dioxide capture, storage, and utilisation (CCSU) technologies should be explored. Further, if any CO$_2$ capture technology is combined with technologies such as power-to-gas (PtG) that operate with renewable energy sources to produce synthetic methane, it would promote a circular economy around the captured CO$_2$ since this would be used as raw material to manufacture E-fuels [7]. Another advantage of this proposal is that the well-developed infrastructure of the NG could be used for methane transport and supply to the vehicles, so the supply chain would not be a drawback in this type of proposal.

CCSU technologies have been demonstrated mainly for their use in power plants, steel, and cement industries, which are the main emitters of CO$_2$ [8]. However, in recent years, research works have been carried out on CO$_2$ capture in mobile sources (vehicles and ships) propelled with traditional ICEs. Several issues have been evaluated in these works: the energy consumption of the CCS system operating with different solvents and sorbents [9–15], the economic impact of the implementation of CCS systems [16–18], the technical feasibility of implementing the CCS systems [19–23]. Also, the properties of the sorbents have been improved to achieve better CO$_2$ capture on board [24]. These research works show that the most widely used CO$_2$ capture techniques have been absorption in the maritime sector and adsorption in road transport. They have also found that CO$_2$ storage is the process that consumes the most energy, and it depends on the CO$_2$ capture rate (CCR), which is why some authors have hybridised an ORC to the CCS system [25–27]. The ORC takes waste heat from the engine's exhaust gases to produce power, thus offsetting the energy demand in the CO$_2$ storage process.

Abbreviations

Adsorption Heat	ΔH_{ads}	Loading Capacity	q
Angular velocity ratio	β_ω	Lower Heating Value	LHV
Area calculated at maximum torque	A_{Tmax}	Mass flow	$\dot{m}$
Area current	$A_{current}$	Mass fraction	x
Carbon Capture and Storage	CCS	Natural gas	NG
Capture, Storage, and Utilisation	CCSU	ORC condenser	ORC-C
Combustion efficiency	η_{com}	ORC evaporator	ORC-E
Compressibility factor	Z	ORC heater	ORC-H
CO_2 capture rate	CCR	ORC pump	ORC-P
CO_2 cooling heat exchanger	$HE–CO_2–C$	ORC expander	ORC-X
CO_2 condenser	CO_2-con	Organic Rankine Cycle	ORC
CO_2 compressor	CO_2-com	Parasitic Load	PL
Cyclopentane	C_5H_{10}	Power-to-Gas	PtG
Density	ρ	Revolutions per minute	Rpm
Displacement volume	dv	Rotary Wheel Adsorber	RWA
Displacement volume ratio	β_{Vol}	Saturation temperature	T_{sat}
Engine load	EL	Specific heat	c_p
Exhaust gases	EG	Pump volumetric efficiency	$\eta_{vol,pump}$
Exhaust gas cooling heat exchanger 1	HE-EG1	Temperature Swing Adsorption	TSA
Exhaust gas cooling heat exchanger 2	HE-EG2	Thermal efficiency	η_{th}
Expander volumetric efficiency	$\eta_{vol,exp}$	Overall heat coefficient	U
Greenhouse gas emissions	GHE	Volumetric efficiency product	$\beta_{\eta v}$
Ideal gas constant	R	Working Fluid	WF
Internal Combustion Engine	ICE	Working fluid density	$\rho_{pmp,in}$

Despite the increased literature on this topic in recent years, most of these research works have been carried out with the ICE operating in a single operating condition, which is suitable for the maritime sector. However, it is far from the actual ICE operation used in freight and passenger road transport vehicles, where the engine must change rpm and engine load constantly to adjust to the required slope or speed, which produces a variation in the mass flow and temperature of the exhaust gases (transient state). These variations affect the performance of any CCS system that could operate in this kind of vehicle due to the variation of the waste heat available in the exhaust gases.

As evidenced in the previous paragraph, there is not enough information in the literature about CCS-ORC systems operation on heavy-duty vehicles whose ICE operates in a transient state. This lack of information is due to the difficulty of obtaining results through simulations of ICE operating in a transient state because of the large number of variables that affect its behaviour. In the same way, experimental tests require a significant investment, which is not easy to assume by a research centre. A way to approach the transient state operation of an ICE through simulations is by sweeping many engines operating conditions, both in rpm and engine load, which would allow knowing the several input conditions of exhaust gases into the CCS-ORC system. With this and through the evaluation of different sorbents, it would establish the CO_2 capture rate (CCR), the energy behaviour, and the first sizing of a CCS-ORC system able to adapt to operate to several operation conditions of an engine.

In this vein, the first objective of this research is to carry out an energy evaluation of a CCS-ORC system designed to capture the CO_2 contained in the exhaust gases of a NG engine operating in several loads and rpm of the engine. For this, two engines (used in freight and passenger road transport and with different displacement volumes) operating at four engine loads in the entire engine rpm are simulated to determine the exhaust gases' temperature, pressure, and composition conditions. The intention of this after the fact is to know if engine size affects the behaviour of the CCS-ORC system. Subsequently, a CCS-ORC system working with temperature swing adsorption (TSA) is simulated. Three sorbents (PPN-6-CH$_2$-DETA, MOF-74Mg and activated carbon)

Table 1
Technical specifications of the F1C and M936G engine.

Engine	M936G [30]	F1C [29,31]
Architecture	In-line 6-cylinder engine	In-line 4-cylinder engine
Aspiration method	Turbocharged with Aftercooler	
Injection	Multipoint	
Valves per cylinder:	4	
Bore [mm]	110	96
Stroke [mm]	135	104
Displacement volume [cm^3]	7700	3000
Connecting Rod Length [mm]	250	220
Compression ratio	17	12.5
Maximum boost pressure ratio	2	1.5
Firing Order	1-5-3-6-2-4	1-3-4-2
Combustion duration [deg]	57	58
Star of combustion BTDC [CAD]	18	19
Brake Power [kW]	222 at 1950 rpm	100 at 3500 rpm
Torque [Nm]	1200 at 1600 rpm	350 at 1500 rpm

and two CCRs (70 and 100 %) are used in the simulations. The aim is to establish the sensibility of the CCS-ORC system to different sorbents and capture rates regarding the energy balance. The second objective of this research is to size and quantify the volume and weight of the CCS-ORC system, thus determining how its installation can affect the useful space of the heavy-duty vehicle. For this, the heat exchange areas of the CCS-ORC system are calculated, and the volume and mass of the sorbent required in an operation of 8 h are estimated. All this work outlines for the first time a mapping of the energy consumption and the dimension of the CCS-ORC system able to adapt to operate in several loads and rpm of the engine, which expands the knowledge paving the way to use CCS in mobile sources as a valuable strategy to mitigate climate change.
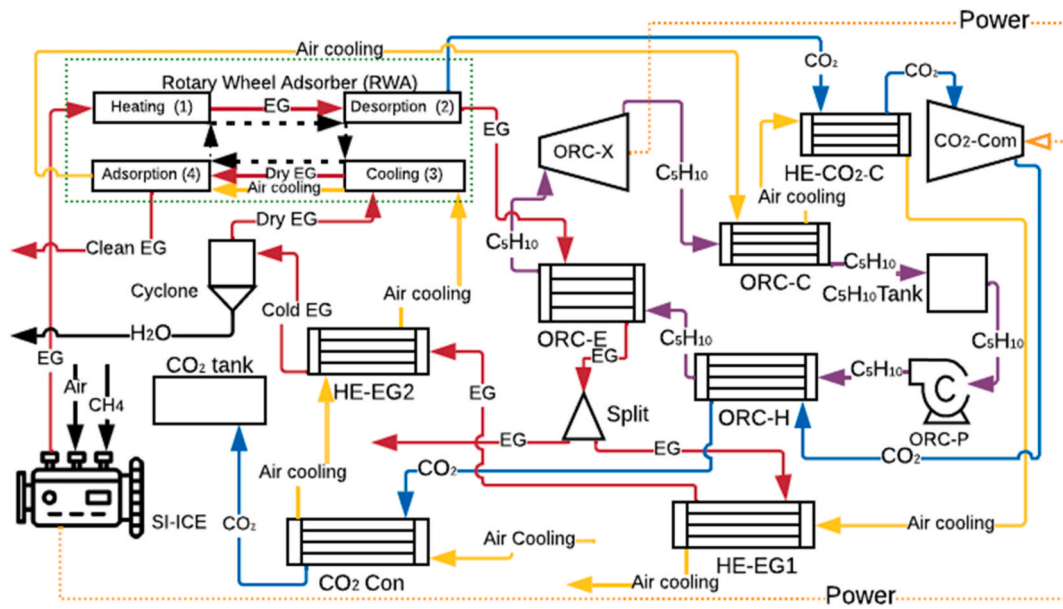
Fig. 1. CCS-ORC system configuration.

2. Methodology

The engine simulations are done in the software AVL boost, and the CCS-ORC system simulations are performed in the software ASPEN +. The following subsections show the procedure developed in this study.

2.1. Engine selection and simulation

Two four-stroke turbochargers natural gas spark-ignition engines with different displacement volumes (dv) are selected for the energy analyses proposed below. These engines are used frequently in passenger and freight road transport. The engines selected are the M936G engine manufactured by Mercedes Benz with a dv of 7700 cc and an F1C engine manufactured by FPT Industrial with a dv of 3000 cc, both engines working with stoichiometric combustion [28,29]. Table 1 lists the specifications of the engines.

The energy simulations for the CCS-ORC system require temperature, pressure, mass flow, and composition of the exhaust gases as input parameters. Both engines are modelled using the software AVL BOOST and values of these parameters are obtained at four partial engine loads (25, 50, 75 and 100 %) in the entire rpm range. The theoretical models used

in the engine are the Woschni heat transfer model for the heat transfer in the cylinders, the simplified model of boost pressure to obtain the air mass flow, the Re-analogy for the heat transfer in the engine ducts and the Heywood, Patton, Nitschke model for the friction. In addition, air at standard conditions (25 °C and 1 atm) and a lower heating value (LHV) of the NG of 48351 kJ/kg were taken as inlet parameters [32–34]. The engine performance results obtained in the engine models and the accuracy between those, and the actual performance curves of the engines provided by the manufacturers [29,30] can be found in previous research [27]. The exhaust gas conditions are also obtained, which are required as input parameters in the CCS-ORC system simulations. These values are consigned in Appendix A and B, the temperature, pressure and mass flow for each species of exhaust gases are shown there. Finally, the mass fraction of the engine exhaust gases obtained in the engine model simulations is 15.4, 12.6 and 72 % for the CO_2, H_2O and N_2, respectively.

2.2. CCS-ORC system

2.2.1. CCS-ORC system configuration

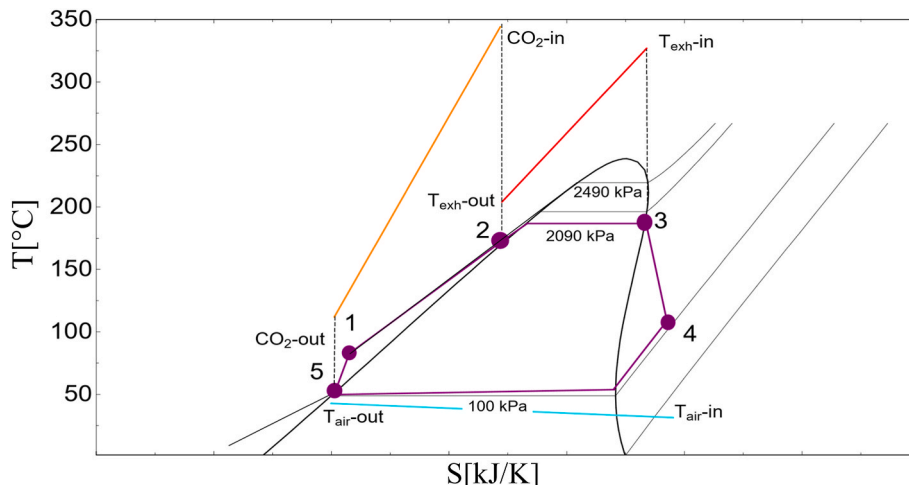The CCS-ORC system was configured using all the high-temperature

Fig. 2. T-S diagram for the ORC.

Table 2
Input parameters for the calculation of the fluid pressure at the ORC-X inlet.

Variable	Value	Unit
Compressibility factor (Z)	0.96	NA
Ideal gas constant (R)	0.1186	kJ/kgK
Saturation temperature (T_{sat})	186.15	°C
WF density at 1 bar ($\rho_{pmp,in}$)	735.3	kg/m³
Expander volumetric efficiency ($\eta_{vol,exp}$)	0.45 [41]	NA
Pump volumetric efficiency ($\eta_{vol,pump}$)	0.8	NA
Volumetric efficiency product ($\beta_{\eta v}$)	0.36	NA
Displacement volume ratio (β_{Vol})	0.76	NA
Angular velocity ratio (β_{ω})	0.2	NA

heat sources to get the most straightforward possible configuration. Moreover, a reduction of 78.1 % for the cooling processes was obtained through a Pinch analysis. Fig. 1 shows the final configuration of all systems integrating the CCS-ORC system proposed for this study.

A rotary wheel adsorber (RWA) is used for the adsorption process (enclosed in green dotted line). The TSA process consists of four stages (black dot lines), represented in Fig. 1. The charged sorbent is heated to a desorption temperature in the first stage so that the CO_2 is released from the sorbent [35] in the second stage. The heat required for these stages is extracted from the exhaust gases coming from the engine exhaust. In the third stage, the sorbent is cooled to the adsorption temperature and is prepared to adsorb CO_2 from the dry exhaust gases in the fourth stage. Air at standard conditions is used for cooling in the last stages.

A basic ORC [36] with two heat sources is integrated into the system to provide the mechanical energy required to compress the CO_2. One source is heat remaining in the exhaust gases after the RWA, and the second is the heat produced in the CO_2 compression. Four additional heat exchangers complete the CCS system to dry the exhaust gases and cool the CO_2. Fig. 1 shows with a different colours each of the flows operating in the systems (exhaust gases - red, CO_2 - blue, air cooling - yellow and ORC working fluid - purple) and the heat exchangers and devices arrangement.

2.2.2. ORC design and working fluid selection

The ORC's working fluid (WF) is cyclopentane (C_5H_{10}). This organic fluid was selected because of the excellent performance results in previous research performed on ORC in ICE [37,38]. On the other hand, C_5H_{10} has a limited environmental impact and low toxicity, is non-corrosive [39], has a low decomposition rate and is thermally stable at temperatures up to 350 °C despite its high flammability despite its high flammability and has a low decomposition rate [40], making it safe for use in this kind of application.

Fig. 2 shows the TS diagram of the thermodynamic states of the WF along the ORC. The ORC circuit begins with preheating the WF in the heat exchanger (ORC-H), thanks to the heat produced during the compression of the CO_2 (1–2 process). Afterwards, the WF is vaporised in the heat exchanger (ORC-E), taking the exhaust gases' waste heat after CO_2 desorption (2–3 process). After, WF flows through an expander (ORC-X) to produce power (3–4 process). Finally, the WF is condensing in the heat exchanger (ORC-C) (4–5 process), and pumping (ORC-P) to begin the cycle again (5–1 process).

The ORC operational pressures were obtained following the procedure developed by Fatigati et al. [41,42] which is based on the permeability concept (equation (1)). Assuming a pressure of 1.5 bar at the outlet of the ORC-X and the inlet pressure in the ORC-X is obtained using equation (2). The meaning of the three dimensionless variables of equation (2) is explained in Ref. [41], and Table 2 shows the used values.

$$\alpha = \frac{\dot{m}_{WF}}{\Delta P} \tag{1}$$

$$P_{in,ex} = ZRT_{sat}\rho_{pmp,in}\beta_{\eta v}\beta_{Vol}\beta_{\omega} \tag{2}$$

Table 3
Parameters and conditions for ORC simulations.

Device	Parameter	Unit	Value	State	Fluid
ORC-C	Inlet pressure	Bar	1.5	Vapour	C_5H_{10}
	U [44]	W/m²K	120→Condensation	NA	Air-C_5H_{10}
ORC-P	Inlet pressure	Bar	1	Saturated liquid	C_5H_{10}
	Isentropic efficiency [46]	NA	0.55	NA	
ORC-H	Inlet pressure	Bar	24.9	Compressed liquid	C_5H_{10}
	U [44,45]	W/m²K	100→Liquid-Gas	NA	C_5H_{10} - C
ORC-E	Inlet pressure	Bar	22.9	Compressed liquid	C_5H_{10}
	h [44]	W/m²K	70→Liquid-Gas 2000→Phase change 35→Gas-Gas	NA	C_5H_{10} - Exhaust gas
ORC-X	Inlet pressure	Bar	20.9	Vapour	C_5H_{10}
	Isentropic efficiency [47]	NA	0.65	NA	

Table 4
Overall heat coefficients for the heat exchangers used in the ORC [44,45,48].

System	Heat exchanger	Process	Fluids	U [W/m²K]
CCS	HE–CO₂–C CO₂-Con	Cooling	CO₂ – Air	100
	HE-EG1 HE-EG2	Cooling Dry	Air – Exhaust gases	

The ORC-X inlet pressure obtained following the described procedure is 20.9 bar; at this pressure, the WF saturation temperature is 184.15 °C. This temperature fits with the critical operation condition in the ORC-E, which is at 25 % engine load and 1000 rpm in the F1C engine (the lowest thermal energy); at this point, the inlet exhaust gases in the ORC-E has a temperature of 222 °C, so it fulfils with ΔT established for its operation (see Table 6). From this, the inlet pressures of the ORC devices are subsequently set from this value. The devices' pressure drops, the heat transfer coefficient (*h*) and the overall heat transfer coefficient (*U*) values are taken from the literature [43–45]. Table 3 shows the parameter values for each device and fluid conditions in the simulations.

2.2.3. Heat exchangers

As seen in Fig. 1, the CCS system has four heat exchangers. The first of them serves to reduce the CO_2 temperature after the desorption process (HE–CO₂–C), the second one is used to condensate the CO_2 (CO₂-con), the third one is used as a first cooling stage of the exhaust gases (HE-EG1), and the last heat exchanger (HE-EG2) finishes cooling and drying the exhaust gases. These heat exchangers utilise the same air cooling that flows through the RWA and the ORC. This information is summarised in Table 4. An overall heat transfer coefficient of 100 W/m²K corresponding to a cooling process in a compact heat exchanger [44,45,48] is considered.

2.2.4. Rotary wheel adsorber (RWA)

The four TSA processes (adsorption, heating, desorption and cooling) are performed on an RWA (green dot lines Fig. 1). This technology operates with VeloxothermTM, developed by Inventys [49]. The advantage of this device is that it is possible to do the TSA cycle in less than 90 s [35], which drives to small equipment sizes. In the simulations, the cooling and heating of the sorbent in the RWA are made by indirect

Table 5

Main physical properties of the sorbents used in the simulations [50,51,53,54].

Sorbent	Adsorption Heat (ΔH_{ads}) [kJ/mol$_{CO2}$]	Loading Capacity (q) [kg$_{CO_2}$/kg$_{sorbent}$]	Selectivity CO_2/N_2	Specific Heat (c_p) [kJ/kgK]	[a]Density (ρ) [kg/m^3]
PPN-6-CH$_2$-DETA	−45.33	0.2354	>10.000	0.985	805
MOF-74-Mg	−37.4	0.27808	209	0.896	914.9
Activated carbon	−25	0.132	11	1.062	1040

[a] Crystallographic density.

Table 6

ΔT and requirements of the heat exchangers in the CCS-ORC system simulations.

Heat exchanger	ΔT between hot and cold fluid [°C] [48]	Fluids	Design condition of the heat exchanger
ORC-C	5	C_5H_{10}-Air	C_5H_{10} outlet as saturated liquid
ORC-E	20	C_5H_{10}-Exhaust gases	C_5H_{10} outlet as saturated vapour
ORC-H	20	C_5H_{10}–CO_2	–
HE–CO_2–C	3	Air-CO_2	–
CO_2-Con	4	CO_2 -Air	CO_2 outlet as saturated liquid
HE-EG1	3	Exhaust gases-Air	–
HE-EG2	3	Exhaust gases-Air	Exhaust gases outlet at 30 °C

contact with air at standard conditions (25 °C and 1 bar) and with the exhaust gases coming from the engine, respectively.

2.2.5. Sorbent selection

Three sorbents are selected for the CCS-ORC simulations: PPN-6-CH$_2$-DETA (PPN onwards), MOF-74-Mg (MOF onwards), and activated carbon (AC onwards). PPN and MOF sorbents present an ultra-high selectivity for CO_2, exceptional adsorption capacity, and low desorption energy, which are suitable physical properties for CO_2 capture (see Table 5) [26,50,51]. AC is a commercial sorbent with ultra-low desorption energy, and several studies have shown that it can be used as a sorbent [52–54].

According to the literature, the suitable desorption temperature that guarantees the greatest amount of CO_2 desorption without sorbent degradation is 150 °C [51] which was chosen in the simulations. On the other hand, the adsorption temperature selected is 30 °C since the exhaust gas is 99 % dry at this temperature, which is ideal for sorbents because they lose CO_2 adsorption capacity with wet exhaust gases [55].

2.2.6. CO$_2$ compression and storage process

Simulations consider the storage of CO_2 as a liquid. According to the CO_2 Mollier diagram, the thermodynamic conditions established in the simulations to do this are a CO_2 pressure of 75 bar and a temperature of 29.35 °C. Regar to the pressure, the CO_2 pressure changed for each sorbent in the simulations due to the impurities of N_2 in the CO_2 stream (due to the selectivity). Consequently, the CO_2 pressure with PPN is 75 bar, with MOF is 77.9 bar and with AC is 85.73 bar; these pressures were calculated using the Dalton Law. The simulations assume an isentropic efficiency of 65 % for the CO_2 compressor (CO_2-Com onwards). The proposed CCS-ORC system configuration has three stages to achieve the CO_2 storage temperature. The first one is done in the HE–CO_2–C using air as cooling fluid before entering the CO_2 compressor. After, the CO_2 is cooled in the ORC-H using the C_5H_{10} as a cooling fluid. The last cooling stage is done in the CO_2-con using atmospheric air as a cooling fluid (See Fig. 1).

2.3. Energy simulations of the CCS-ORC system

The energy analysis of the CCS-ORC system aims to quantify by simulations the penalty over the engine in power terms that would induce their operation. Thus, it is necessary to know the heat and areas of the heat exchangers and the power consumption of the expander, pumps and compressors. All of this is per each rpm and engine load condition. The following shows the assumptions and the procedure developed in the simulations.

2.3.1. Assumptions

The following assumptions are considered in the CCS-ORC system simulations: (i) there are no mass losses in pipes, devices, and connections; (ii) there are no pressure drop losses in the pipes; (iii) heat losses in pipes are negligible; (iv) exhaust gases are non-corrosive during the heat transfer; (v) steady-state conditions in the simulations; (vi) inlet air for cooling at standard conditions; (vii) heat exchanger are simulated in counter-flow type.

2.3.2. Procedure in simulations

Simulations are performed for two CCR conditions (70 and 100 %), at 25, 50, 75 and 100 % of engine load and in the entire rpm range. For both CCR conditions, the areas of the heat exchangers of the CCS-ORC system must first be known. These areas were determined at maximum engine torque. The cooling air mass flow is obtained when the sorbent is cooled at 30 °C and are fulfil the design condition is reached of the heat exchanger and the selected ΔT (from the literature) between the hot and cold fluid in each heat exchanger is met (see Table 6).

The ORC cycle was simulated so that the WF at the ORC-X outlet was always saturated vapour (see Fig. 2), which fixes the maximum mass flow of the WF for each engine condition in the simulations, thus obtaining the maximum power production. Also, the values for the heating, cooling, desorption and adsorption heat developed in the RWA are introduced for each simulation (Appendix C, D, E and F). These values are calculated using equations (3)–(5). The ΔT in these equations is 120 °C, which is obtained as the difference between desorption temperature (150 °C) and exhaust gas drying temperature (30 °C).

$$\dot{Q}_{heating} = CCR x_{CO_2} \dot{m}_{EG} \Delta T \left(c_{p-CO_2} + \frac{c_{p-CO_2}}{q} \right) \tag{3}$$

$$\dot{Q}_{cooling} = \frac{c_{p-CO_2} CCR x_{CO_2} \dot{m}_{EG} \Delta T}{q} \tag{4}$$

$$\dot{Q}_{desorption/adsorption} = CCR x_{CO_2} \dot{m}_{EG} \Delta H_{des} \tag{5}$$

This procedure allows us to calculate the power consumption of the ORC-P and the CO_2 compressor, the power production of the ORC-X, the air mass flow of the fan used to cool the CCS-ORC system, the WF mass flow in the ORC and the heat flux of all heat exchangers in the rest of the engine operational points.

As is expected, for the other simulation points, the values of the areas of heat exchangers change. At thermal operating conditions higher than maximum torque, these areas are equal to the calculated since the software controls this by increasing the cooling flow or limiting the WF flow. By contrast, at lower thermal points than the maximum torque, the heat exchanger areas present a lower value, which is good since if a larger area is required, this would indicate that the heat transfer process could not develop properly. The areas always were controlled and verified using equation (6), whose value must always be equal to or greater than zero.

$$A_{difference} \, (\%) = \left(\frac{A_{Tmax} - A_{current}}{A_{Tmax}} \right) 100 \tag{6}$$

Table 7

Heat exchangers areas obtained in the simulations.

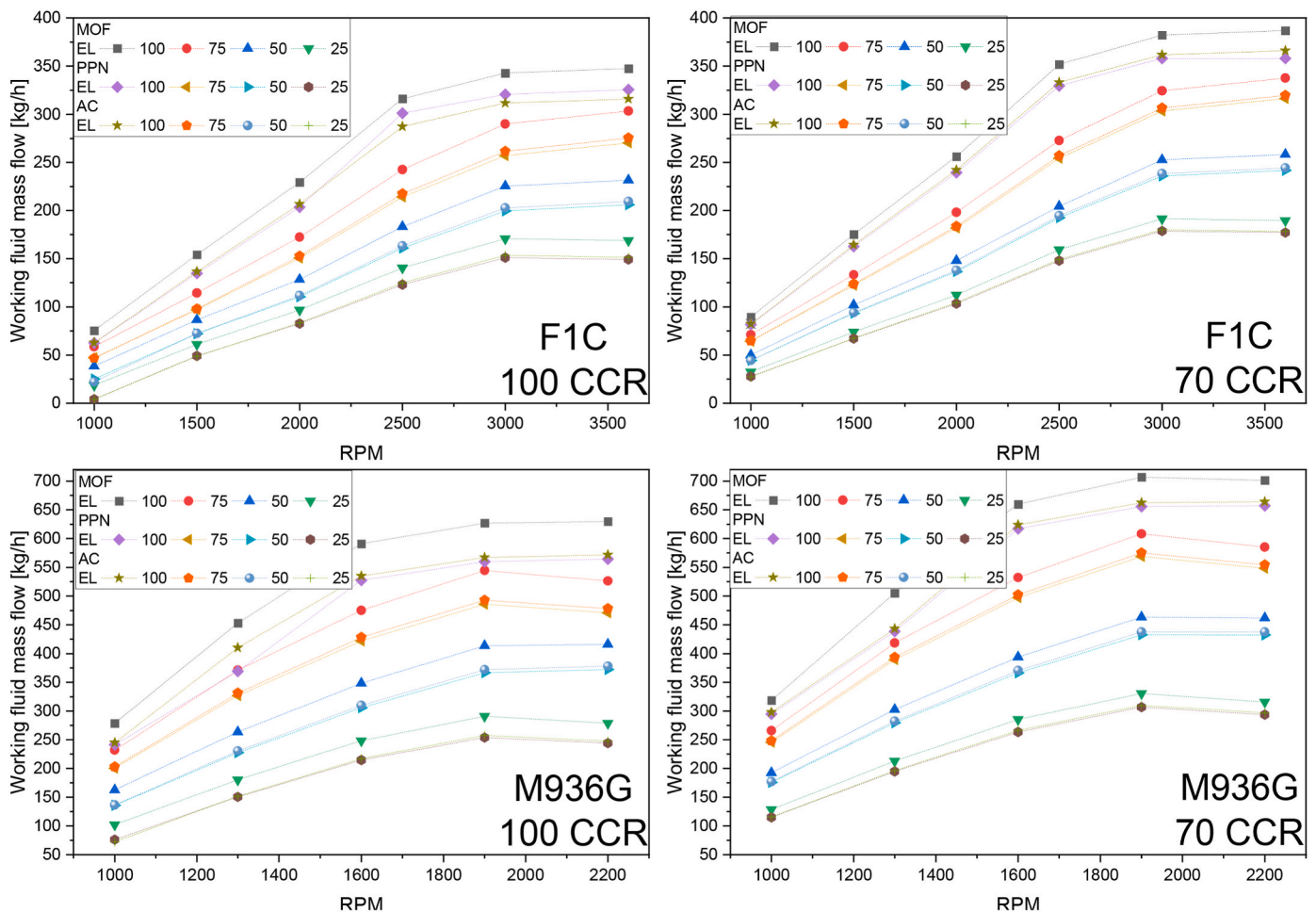| Engine	Sorbent	CCR	ORC-C [m²]	ORC-E [m²]	ORC-H [m²]	HE–CO₂–C [m²]	CO₂-Con [m²]	HE-EG1 [m²]	HE-EG2 [m²]	Total [m²]
M936G	MOF	70	17.90	8.17	0.59	0.67	1.87	18.36	11.58	59.13
	PPN		16.53	8.16	0.57	0.67	1.82	18.74	10.18	56.68
	AC		16.71	7.95	0.63	0.73	1.96	17.99	10.25	56.21
	MOF	100	15.61	7.66	0.75	0.95	2.54	25.37	13.02	65.91
	PPN		13.77	7.59	0.72	0.95	2.46	25.30	11.20	62.01
	AC		13.97	7.17	0.79	1.05	2.64	24.23	11.31	61.16
F1C	MOF	70	9.56	4.27	0.31	0.35	0.98	9.61	6.12	31.19
	PPN		8.84	4.27	0.30	0.35	0.96	9.81	5.38	29.91
	AC		8.93	4.16	0.33	0.38	1.02	9.41	5.42	29.66
	MOF	100	8.36	4.02	0.50	2.54	1.33	13.30	6.88	36.93
	PPN		7.92	4.01	0.39	0.50	1.30	13.34	6.40	33.86
	AC		7.51	3.79	0.42	0.55	1.38	12.72	5.99	32.35

Fig. 3. C_5H_{10} Mass flow under the two CCR conditions and over the entire rpm range.

3. Results and analysis

This section presents the results obtained from the simulations of the CCS-ORC system. Initially, the results of the operational parameters of the CCS-ORC system (heat exchanger areas and fluid mass flows) are presented. Then, energy performance as power production and consumption by the devices and the penalisation over the engine by the CCS-ORC system operation is presented. Finally, the mass and volume of the sorbent for an ICEv operation of 8 h are quantified to establish the required weight and volume in the RWA and the volume of the heat exchangers to get the spatial dimension of the CCS-ORC system.

3.1. Heat exchanger areas

Table 7 shows the values of the heat exchanger areas of the CCS-ORC system that are obtained in the simulations. Both engines' heat exchanger areas of the CCS-ORC system show similar trends. The results show that the ORC-E and ORC-C heat exchanger areas are larger for a 70 % CCR than a 100 % CCR. For the ORC-E and ORC-C exchangers, it can be explained because of the higher WF mass flow needed to take advantage of the heat in the exhaust gases. This remaining heat is higher due to a lower heat requirement in the heating and desorption processes at 70 % of CCR. On the contrary, the HE-EG1, HE-EG2, ORC-H, HE–CO₂–C and CO₂–C areas are lower for the lower CCR, caused by a smaller mass flow of exhaust gases and CO_2.
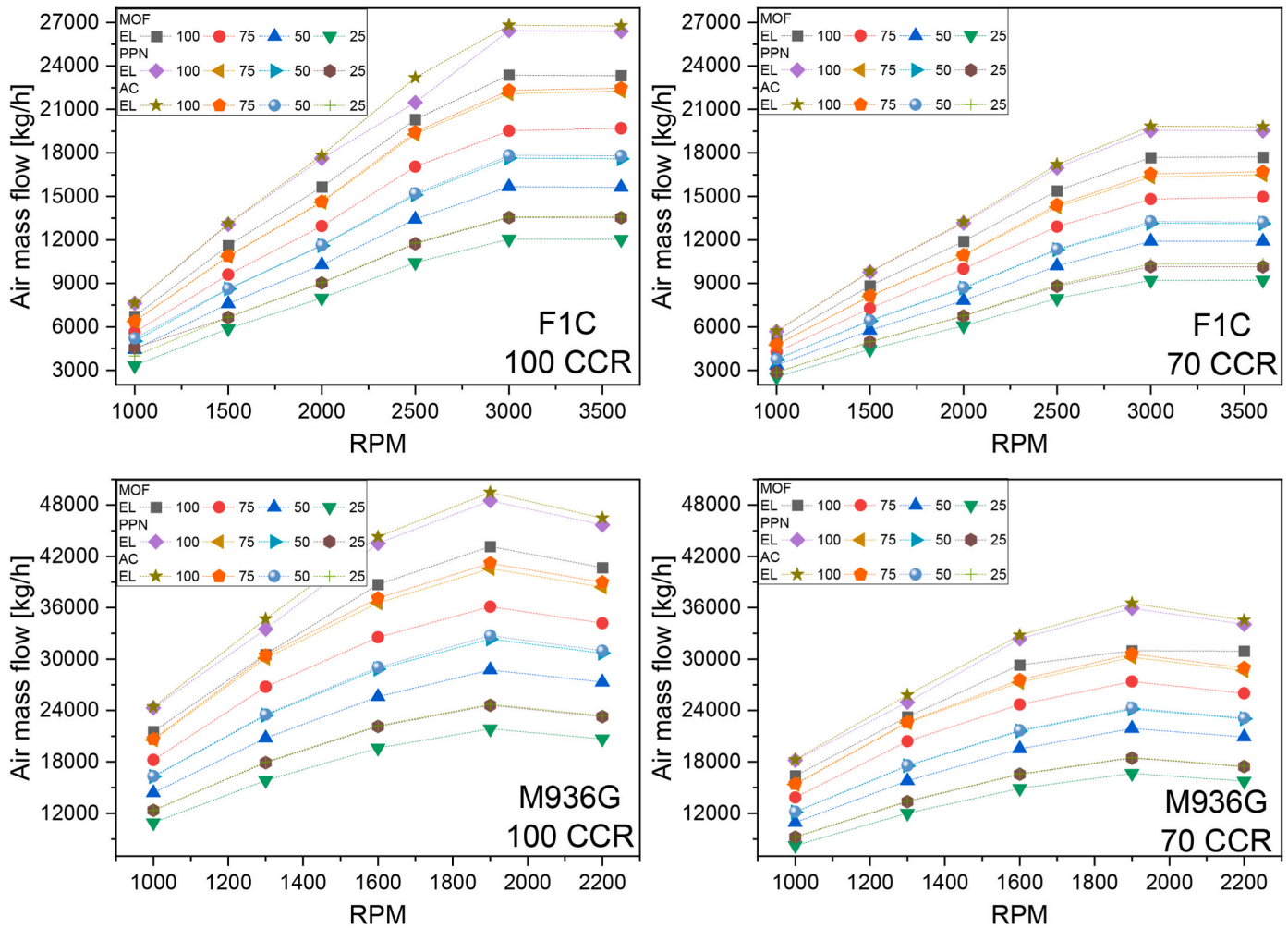
Fig. 4. Cooling air mass flows in the CO$_2$-Con, the RWA, the ORC-C, the HE–CO$_2$–C and the HE-EG1 in the entire F1C and M936G engine rpm.

The effect of the sorbent in the heat exchanger areas of the CCS-ORC system can be seen in the CO$_2$-Con. For instance, with MOF operation, there is a difference between the heat exchanger areas of 2.5 % at 70 % of CCR and 2.7 % at 100 % of CCR regarding PPN operation. This difference is due to the selectivity of the sorbent. The MOF-74-mg has a lower selectivity than the PPN-6-CH$_2$-DETA, which makes the CO$_2$ mass flow contain impurities of N$_2$ which change the heat transfer parameters producing an increase in the area of the CO$_2$-Con. This same behaviour can be seen with the AC sorbent, whose selectivity is the lowest of the three sorbents.

Finally, the area of the HE-EG2 is, on average, 11.2 % greater with MOF operation regarding PPN and AC operation both for the two CCRs and the two engines. This result is because, in MOF operation, the cooling air mass flow is the lowest obtained due to the lowest heat of cooling and adsorption with this sorbent, which produces that this heat exchanger requires a larger area.

3.2. Mass flows of C$_5$H$_{10}$ and air

Fig. 3 shows the C$_5$H$_{10}$ mass flows in the ORC simulations. It can see a higher C$_5$H$_{10}$ mass flow in 70 % CCR than in 100 % CCR in both engines and with all sorbents at the highest engine load (EL). It can be explained as in the 70 % CCR case, less heat from the exhaust gases in the sorbent's heating and desorption process is consumed mainly due to less sorbent and CO$_2$ mass involved in the processes. However, as mentioned before, this rise in the WF mass flow increases the heat exchanger areas of the ORC-E and ORC-C, regarding the CCS-ORC system operation at 100 % of

CCR.

Considering sorbents, the MOF operation always presents a higher C$_5$H$_{10}$ mass flow than the PPN and AC operation. This result is because the heating and desorption heat with MOF operation is less than the PPN operation. At the same time, the difference between MOF and AC operation is due to the higher selectivity of the MOF-74-mg regarding the AC that involves a fewer mass of the sorbent and, hence, a low heating heat.

Fig. 4 shows the cooling air mass that flows through the CO$_2$-Con, the HE-EG2, the RWA, the ORC-C, the HE–CO$_2$–C and the HE-EG1 on both SI-ICE, both CCRs and for the three sorbents. It can see that the highest cooling air mass flow values appear at a CCR of 100 %. These results are due to more CO$_2$ mass for condensing and more demand for cooling the RWA since higher heat is consumed from the exhaust gases in the RWA at 100 % of CCR than at 70 % of CCR. For this reason, the air mass flow with PPN and AC operation is higher than with MOF operation under whatever engine load and rpm because of its lowest desorption heat.

3.3. Energy consumption of the CCS system devices

Understanding the power usage of the different devices within the CCS-ORC system is crucial for quantifying power losses. This section presents the findings regarding the power generated by the ORC-X and the power consumed by parasitic loads, which include the combined power from the CO$_2$-com, the ORC-P, and the air fan utilised in the cooling processes (Equation (7)). The power consumption of the air fan is determined by selecting fans from the EBMPAPST company's online
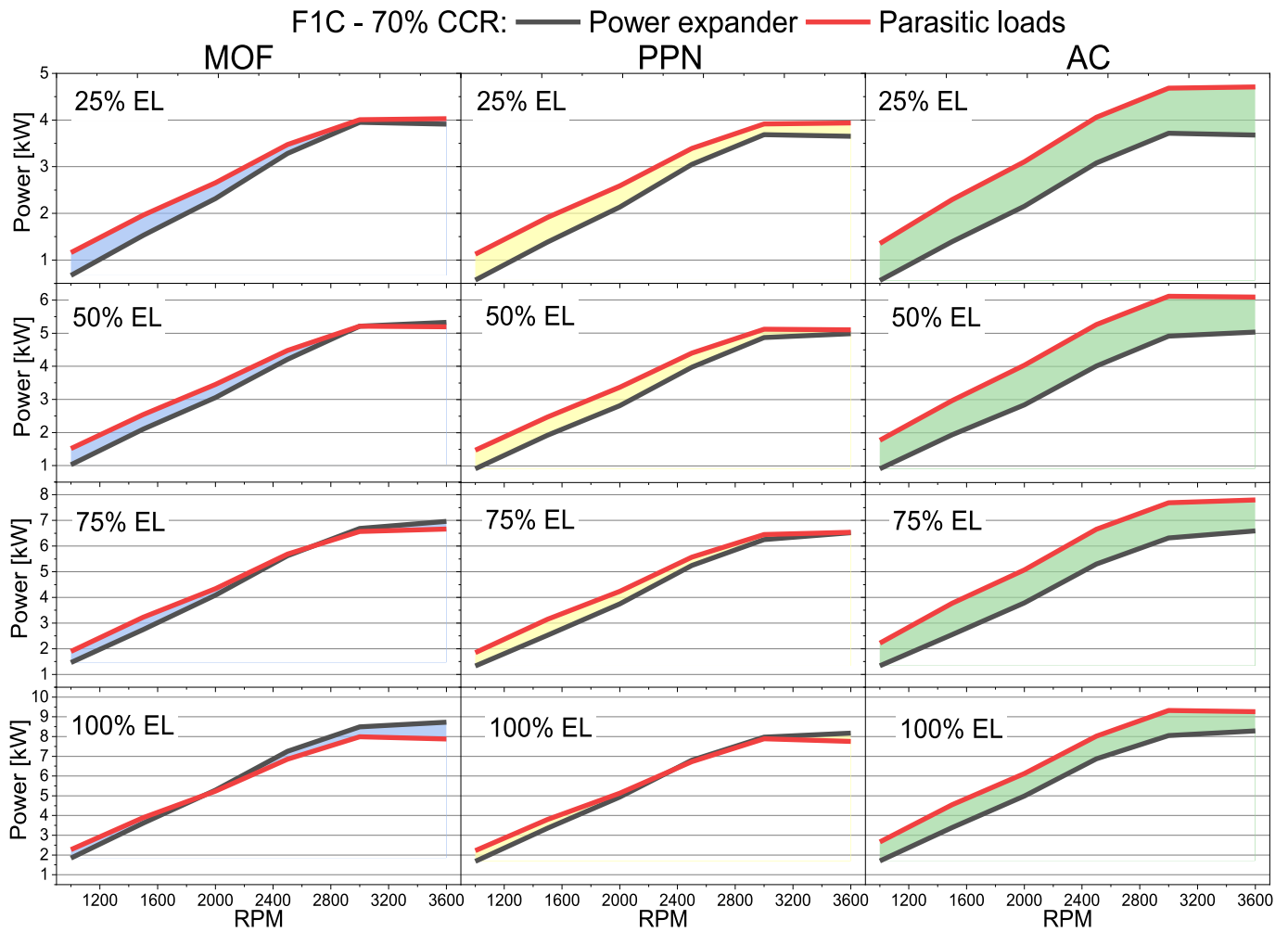
Fig. 5. Power production by the ORC and parasitic loads by the CCS-ORC system in the F1C engine.

catalogue [51] that align precisely with the simulated air mass. Additionally, the section presents the percentage of engine power utilised by the CCS system due to its operation.

$$\dot{W}_{parasitic\ loads} = \dot{W}_{pump} + \dot{W}_{compressor} + \dot{W}_{fan} \qquad (7)$$

3.3.1. Power production and parasitic loads in the CCS-ORC system

The following figures show the difference between the power produced by the ORC-X and the parasitic loads of the CCS-ORC system at 70 and 100 % CCR in both engines and for all sorbents. Fig. 5 shows the parasitic loads power consumption and power production of the ORC-X at 70 % of CCR with all sorbents in the engine F1C. There can be seen that with MOF operation, the parasitic loads are covered by power produced in the ORC-X at 100 % of the engine load from 2000 rpm; at 75 % of the engine load, the ORC-X covers the parasitic loads from 2800 rpm, and at 50 % of the engine load, the parasitic loads are covered from 3200 rpm.

During PPN operation, the ORC-X generates sufficient power to compensate for the parasitic loads at 100 % and 75 % of the engine load, starting from 2400 to 3600 rpm, respectively. However, in the case of AC operation, the parasitic loads are never fully compensated due to the elevated pressure needed for CO_2 liquefaction. The lower AC selectivity primarily causes this limitation. Furthermore, when utilising any sorbent, the power generated by the ORC-X is unable to meet the requirements of the parasitic loads at 25 % of the engine load. The main reason for this is that, under this specific engine load condition, the exhaust gases contain the lowest level of thermal energy.

Fig. 6 shows the difference between the power produced by the ORC-X and the parasitic loads of the CCS-ORC system at 100 % CCR in the F1C engine with all sorbents. With this condition, the CCS-ORC system can not cover the parasitic loads with any sorbent. This behaviour was anticipated because, as the CCR increases, the mass flow of the working fluid (WF) in the ORC decreases, resulting in lower power production by the ORC-X. Additionally, the power consumption of the CO_2 compressor rises due to the increased mass of CO_2 being captured.

In the M946G engine at a 70 % CCR (Fig. 7) in MOF operation, the parasitic loads are covered at 100 % of the engine load from the maximum torque (1500 rpm), 75 % of the engine load from 1700 rpm, and 50 % of the engine load from maximum power (2000 rpm). With PPN operation at 100 % of the engine load, the parasitic loads are covered from 2000 rpm and in the rest of the engine loads, the parasitic loads are not covered. Fig. 8 depicts a similar trend with all the sorbents studied at a CCR of 100 %, resembling the behaviour observed in the F1C case.

3.3.2. Engine power percentage consumed by the CCS system

Figs. 9 and 10 show the power percentage required from the engines to operate the CCS-ORC system across various rpm and engine load conditions, sorbents, and selected carbon capture rates (CCRs). These figures demonstrate that, regardless of the sorbent, CCR, or engine rpm, the most significant impact on the engines occurs at 25 % of the engine load. However, this penalty decreases as the engine load increases, and the ORC system can even deliver excess power, as with MOF operation at a 70 % CCR.
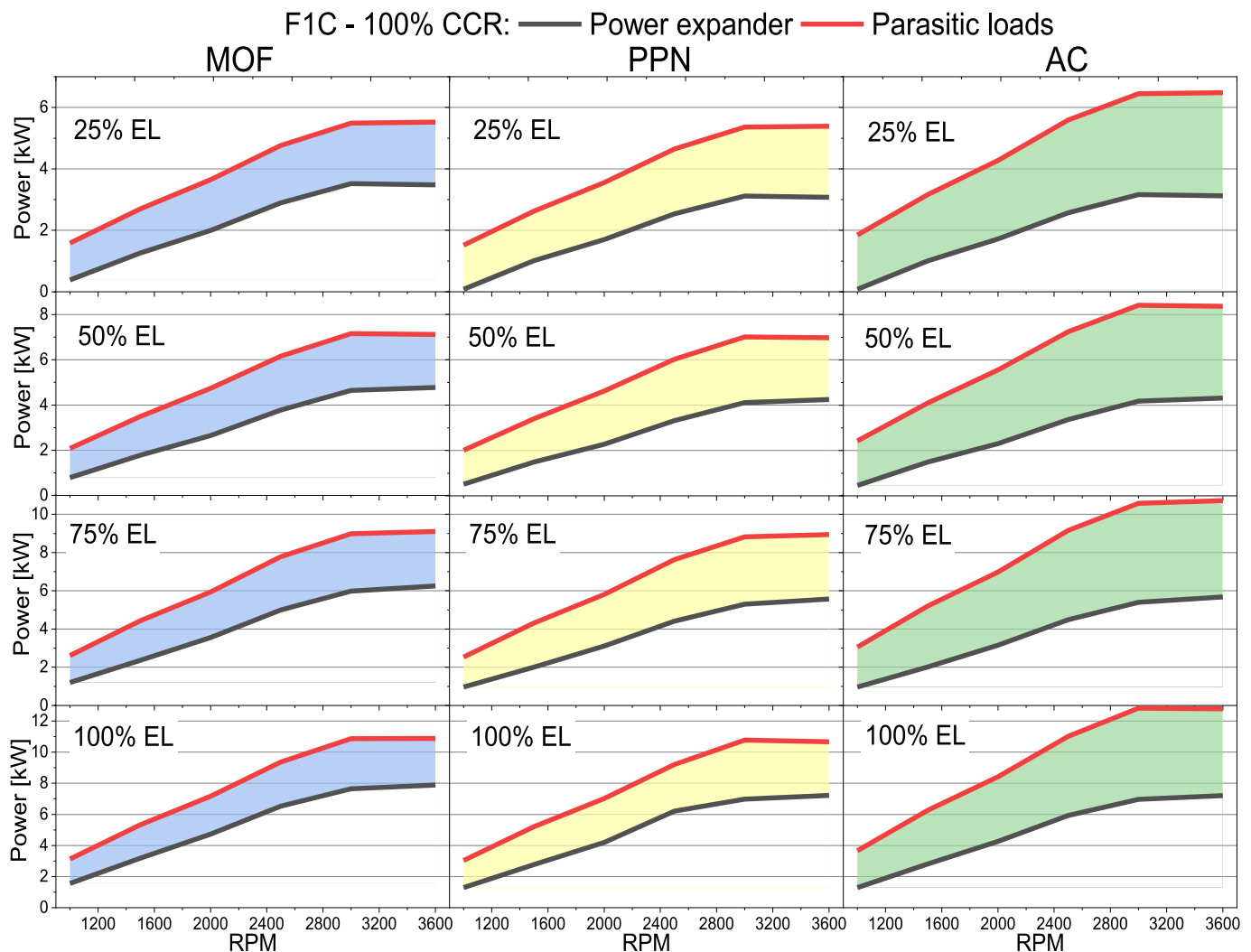
Fig. 6. Power production and parasitic loads in the CCS system with MOF-74-Mg and CCR of 100 % in the F1C engine.

As anticipated, the penalty percentage of the CCS-ORC system on the engine follows the AC operation > PPN operation > MOF operation sequence. The main reason for this is the reduced need for heating and desorption heat in MOF operation compared to other sorbents. The penalty percentage values of the CCS-ORC system on the F1C engine, at a 70 % CCR, range from 0 % with MOF operation to 10.8 % with AC operation. At a 100 % CCR, these values range from 2.2 % with MOF operation to 23.5 % with AC operation.

Likewise, for the M936G engine, at a 70 % CCR, the penalty percentage values range from 0 % with MOF operation to 7.1 % with AC operation. At a 100 % CCR, the penalty percentage values range from 1.9 % with MOF operation to 13.1 % with AC operation.

The values in the above figures show that the CCS system has a more significant penalty on the smaller engine size, irrespective of the sorbent used. In addition, at 25 % of the engine load, the highest penalty percentage values are obtained regardless of the sorbent since all the engines' power output is at its lowest point during this load condition, thereby amplifying the penalty percentage of the CCS system on the engines.

3.4. Weight and volume of the CCS-ORC system

The limited space within an ICEV poses a significant challenge for installing a CCS-ORC system. Hence, it is crucial to determine the mass and area needed to incorporate a CCS-ORC system into the vehicle. This estimation involves calculating the mass and volume of the sorbent within the CCS-ORC system. The calculation procedure assumes a CCR of 100 % for both engines, an 8-h operation with 48 cycles of desorption and adsorption (each lasting 10 min), and an engine load of 75 % at the maximum torque RPM. The results of these calculations are presented in Table 8.

Finally, the mass and volume of the CCS-ORC system are estimated. The weight and volume of commercial compressors that meet the mass flow of CO_2 obtained in both engines are taken for this [56]. Concurrently, the weight and volume of a screw expander operating in the power ranges obtained in the simulations are taken from the literature [57]. Subsequently, the volume of the heat exchangers is obtained considering an area density (β) of 100 m^2/m^3 and the corresponding weight is extrapolated from analogous studies [58]. Finally, the tanks and ancillary systems' weight of the CCS-ORC system is estimated at 200 kg for the M936G engine and 120 kg for the F1C engine.

Based on the results, the CO_2 mass captured from the exhaust gases during an 8-h operation weighs 710 kg and 373 kg for the M936G and F1C engines, respectively. In its liquid state, the storage of this captured CO_2 requires 0.93 m^3 and 0.49 m^3 of volume for the M936G and F1C engines, respectively. The sorbent mass needed to capture CO_2 in the M936G engine amounts to 53.2 kg, 62.9 kg, and 112.1 kg for MOF, PPN, and AC operation, respectively, which translates to a sorbent volume
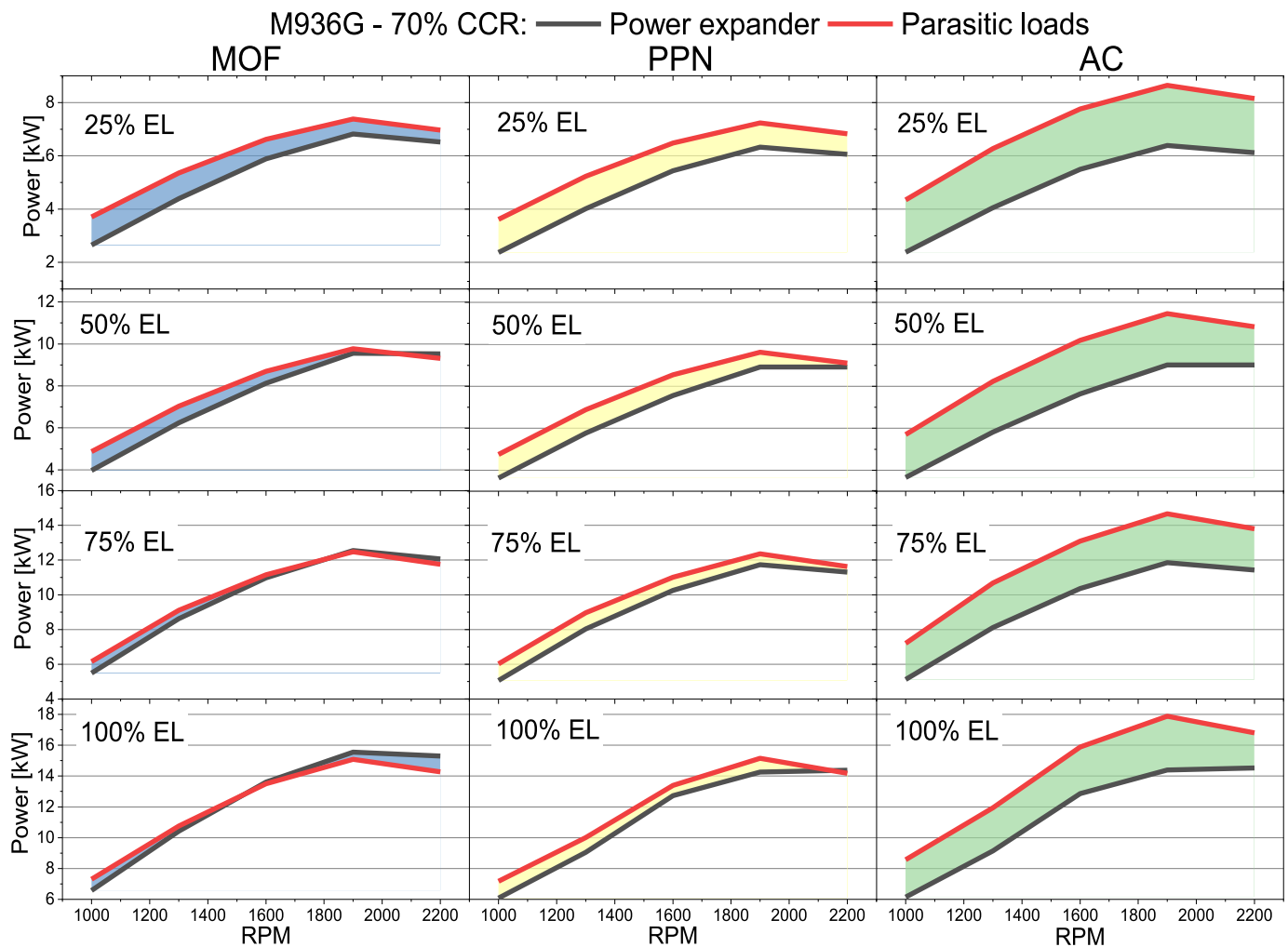
Fig. 7. Power production and parasitic loads in the CCS system with PPN-6-CH$_2$-DETA and CCR of 70 % in the M936G engine.

(RWA volume) of 0.116 m^3, 0.156 m^3, and 0.224 m^3. For the F1C engine, the required sorbent mass is 28 kg, 33 kg, and 58 kg for MOF, PPN, and AC operation, respectively. The corresponding sorbent volumes are 0.061 m^3, 0.082 m^3, and 0.118 m^3 for MOF, PPN, and AC operation, respectively. These results indicate that the selectivity parameter has the most significant impact on the weight of the CCS-ORC system. Consequently, the operation with AC, which has the lowest selectivity among the chosen sorbents, resulted in the highest weight for the CCS-ORC system.

The average weight and volume of the CCS-ORC system obtained are 1200 kg and 2.11 m^3 for the M936G engine vehicle and 695 kg and 1.12 m^3 for the F1C engine vehicle. Fig. 11 depicts the weight distribution of components within the CCS-ORC system. There, it can be seen that the CO$_2$ compressor is the equipment exerting the greatest influence on the total weight of the CCS-ORC system in both ICEVs, with its values ranging between 39.7 % and 45.4 % of the overall weight. Conversely, the heat exchangers, the RWA, and the tanks and auxiliaries exhibit comparable weight contributions across both engines, averaging 19.8 %, 17 %, and 6 %, respectively. Notably, the ORC-E exhibits a higher proportional weight in the F1C engine than the M936G; this disparity arises from using the same expander for both cases. The decision to use the same ORC-E in both ICEVs is due to its volume barely representing 2.7 % of the total volume of the CCS-ORC system, and it has a good performance with the mass flows of the WF obtained in both engines [58].

4. 4analyses

The results show that the volume obtained for the CCS-ORC system with a CCR of 100 % represents scarcely 3.4 % of the total volume of a bus that uses the M936G engine and the space that the CCS-ORC system would occupy of a vehicle using an F1C engine represents 10.2 % of the total volume of the vehicle. These values can be diminished through a thorough design process for the heat exchangers, Although the values in the present research coincide with those reported in the literature [25, 57]. This process would consider factors such as the type of heat exchanger, geometric configuration, construction material, β, and other design parameters. Therefore, installing the CCS-ORC system in a heavy-duty vehicle is technically feasible since it barely affects its workspace. These values are even 15.6 % lower than the volume occupied by an electric battery of a heavy vehicle [59]. Regarding the CCS-ORC system weight, this could lead to an increase in fuel consumption. However, this extra weight in a heavy-duty vehicle would not imply a significant increase in fuel consumption [60]; consequently, the operation cost of the vehicle would hardly be affected by this variable.

However, the engine must augment fuel consumption to offset the parasitic loads the ORC fails to address. This is despite the crucial role played by the ORC in mitigating the penalty of the CCS system over the engine, which can be up to 11 % higher in the absence of the ORC. For this reason, it is necessary to quantify the extra fuel mass that the engine needs to cover the difference between the parasitic loads (PL) caused by the CCS system and the power produced by the ORC-E (PE); equation (8)
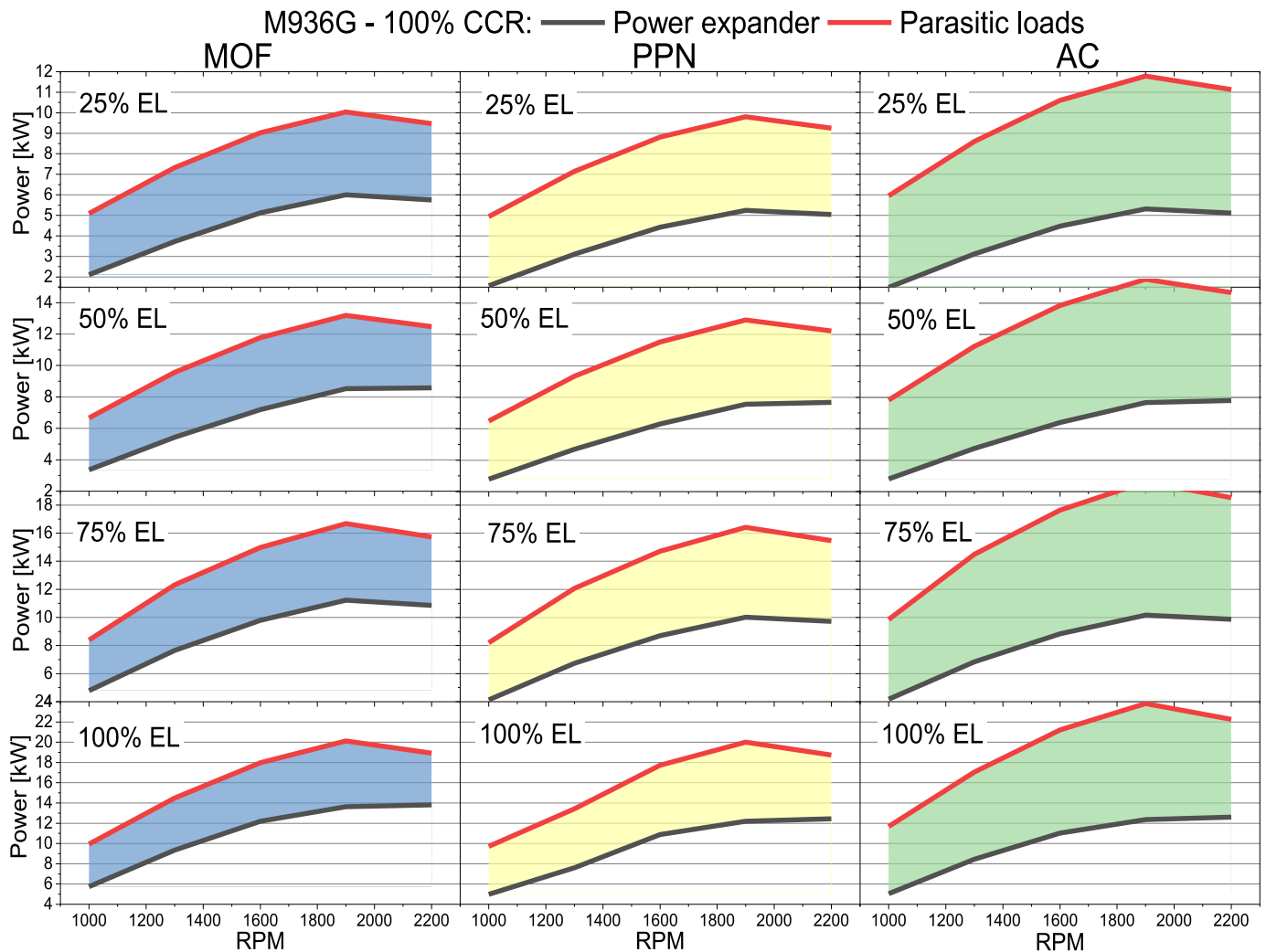
Fig. 8. Power production and parasitic loads in the CCS system with MOF-74-Mg and CCR of 100 % in the M936G engine.

is used. In this equation, the η_{com} is the combustion efficiency and η_{com} is the engine's thermal efficiency. These parameters are obtained from the engine simulations, whose values are listed in Appendix G and H. The assumptions for the calculations are the same as for the mass and volume calculation made in section 3.5 (75 % of engine load, at maximum torque and 8-h of operation). The results obtained are reported in Table 9.

$$m_{fuel} = \frac{28800(PL - PE)}{\eta_{com}\,\eta_{th}LHV} \quad (8)$$

As seen in this table and as expected, the highest increase in the fuel mass is at 100 % of CCR and in AC operation, with values of 7.5 % in the M936G engine and 6.14 % in the F1C engine. However, at 70 % of CCR, the rise in the fuel mass with the MOF and PPN sorbents is almost marginal, with values less than 0.52 %. Even the fuel mass increase at 100 % of CCR could be covered if the transport sector must pay a carbon emission tax.

In the present research, the detail of the CCS-ORC system in the simulations was improved. Also, the WF mass flow calculation was changed and the U in the heat exchangers was updated (to get a more realistic process). As a result of these changes, the value obtained of the ORC efficiency was 11.7 %, which continues to coincide with the reported ORC efficiency in the literature [61,62]. In addition, as can be seen in Fig. 12, it was achieved that the size of the engine does not have a significant interference in the operation of the CCS-ORC system since the

percentage of the power of the parasitic loads covered by the ORC vary only with the type of sorbent used. The main difference between one engine and another at 70 % of CCR is 1.3 %, and 5.8 % at 100 % of CCR. Finally, it is observed that at 100 % CCR, the ORC can cover 42 % of the parasitic loads with AC and with MOF up to 60 %, while at 70 % CCR, this percentage goes from 73 % with AC to 92 % with MOF.

Fig. 13 shows the energy consumption of the capture process. As can be seen in this figure, the maximum energy consumption is obtained with CCR of 100 % in the F1C engine at 25 % of engine load and the lowest rpm engine, whose maximum value is 631 kJ/kgCO$_2$ in AC operation; with PPN operation, the value is close to 510 kJ/kgCO$_2$ and with MOF operation 429 kJ/kgCO$_2$. With the same CCR, these values are nearly 12 % lower in the M936G engine. These values coincide with the values reported by Kim et al. [63], who simulated an onboard CO$_2$ capture system with TVSA in diesel heavy-duty. Additionally in the literature, the energy consumption values for TSA, PSA and VSA are higher than 700 kJ/kgCO$_2$ at 90 % of CCR [64,65] and, with amine-scrubbing, are higher than 2500 kJ/kgCO$_2$ [66,67]. Therefore, the energy consumption of the CCS-ORC system is observed to be lower than the values reported in existing literature. This reduction is due to the taking advantage of waste heat from exhaust gases through the ORC. So, the findings reported herein and, in the literature, suggest that this kind of system, which is still in its design and simulation phase, has good prospects for its experimental development.

In analysing the behaviour of engines, the CCS-ORC system can
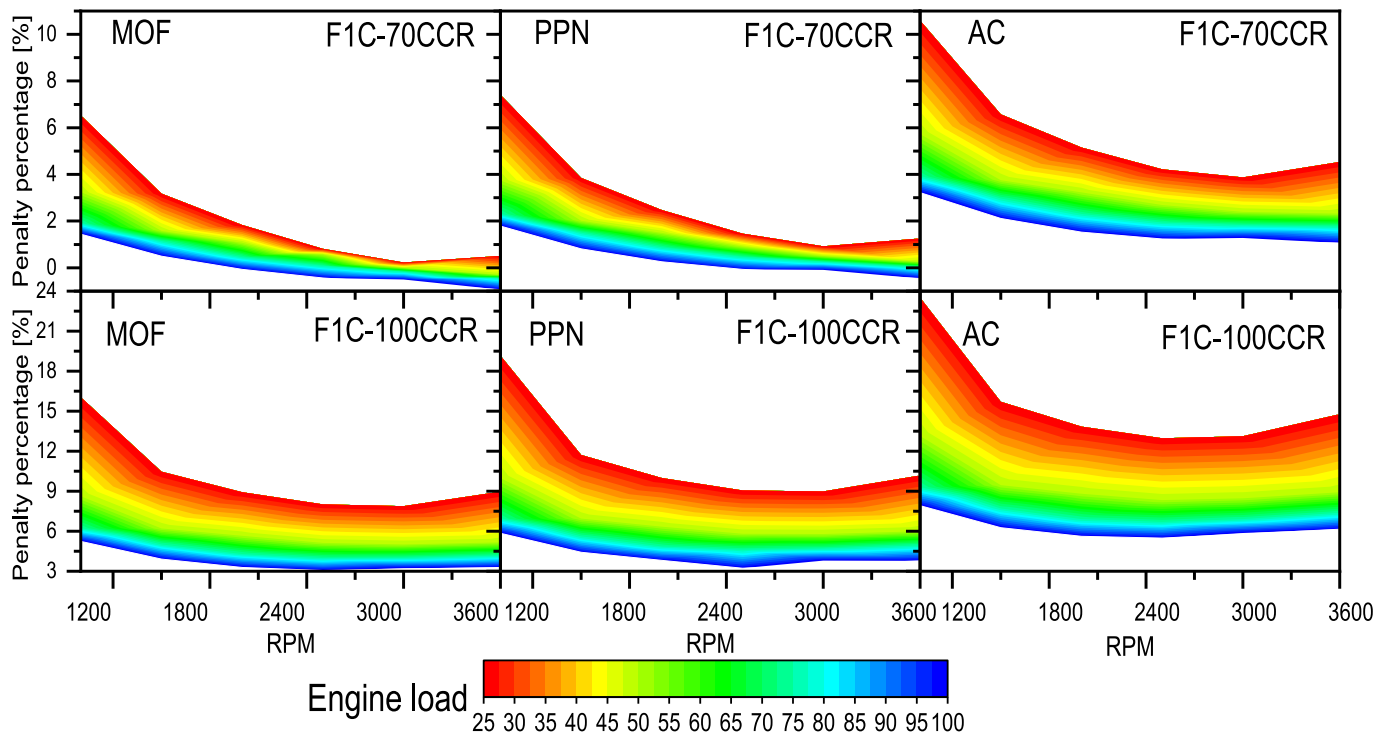
Fig. 9. Power percentage consumed by the CCS system operating in the M936G engine.
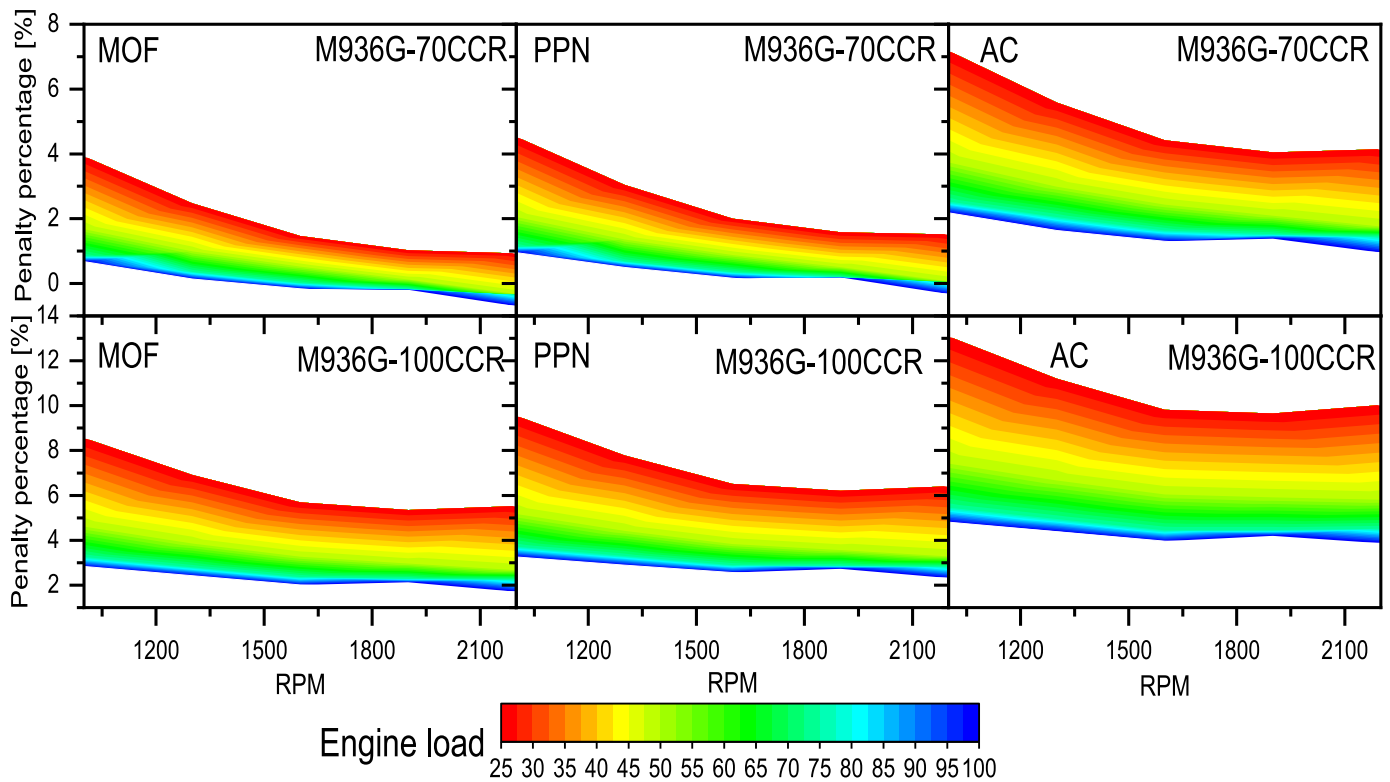
Fig. 10. Power percentage consumed by the CCS system operating in the F1C engine.

operate when there are engine accelerations (rise of load or rpm engine or both). Since the exhaust gas temperature increases due to the fuel enrichment in the engine charge (fuel-air mixture). This behaviour benefits the CO_2 desorption and the correct functioning of the ORC since

there is more waste heat in the exhaust gases available to take advantage of. On the contrary, when there are engine decelerations (reduction in load or rpm of the engine or both), the CCS-ORC system operation could be affected since there is a decrease in the fuel in the engine charge,

Table 8
Mass and volume of sorbent for 30 min of operation at 25 % of EL at the RPM of maximum torque.

Engine	M936G			F1C		
Sorbent	MOF	PPN	AC	MOF	PPN	AC
Exhaust mass [kg]	4610.07			2417.76		
CO_2 mass captured [kg]	710.13			373.16		
CO_2 volume [m³]	0.93			0.49		
Sorbent mass (RWA weight) [kg]	53.2	62.9	112.1	28	33.0	58.9
[a]Sorbent Volume (RWA volume) [m³]	0.116	0.156	0.224	0.061	0.082	0.118
CO_2 compressor weight [kg] [56]	540			276		
CO_2 compressor volume [[m³] [56]	0.366			0.183		
ORC-E weight [kg] [57]	127.8					
ORC-E volume [m³] [57]	0.03					
Heat exchangers volume [m³] [58]	0.66	0.62	0.61	0.35	0.34	0.32
Heat exchangers weight [kg] [58]	257	241.8	238.5	135.7	132.1	126.2
[b]Weight of CCS-ORC system [kg]	1178	1172.5	1218.4	687.4	688.9	708.9
Total Volume of CCS-ORC system [m³]	2.11	2.11	2.17	1.11	1.12	1.14

[a] Calculated with 50 % of the crystallographic density.
[b] Without the CO_2 mass.

reducing the exhaust gas temperature. This condition limits the desorption of CO_2 by not achieving the minimum desorption temperature, and in the ORC, there would be less waste heat available to take advantage of.

5. Conclusions

This paper introduces an innovative CCS-ORC system to mitigate CO_2 emissions from heavy-duty vehicles. The proposed system involves harnessing waste heat from the exhaust gases coming from an ICE to desorption of CO_2 and produce power into an ORC to supply the power demand in the CO_2 compression stage and cooling of all systems (see Fig. 1). The study within the framework of an energy analysis encompasses different case scenarios, wherein the sorbent is changed (PPN-6-CH_2-DETA, MOF-74-Mg, and activated carbon) and engine size (M936G

and F1C). The evaluation is carried out at four partial engine loads, the whole rpm range, and with two CCRs (70 and 100 %). The results provide valuable information on the energy requirement and size of the different components of the CCS-ORC system and the energy consumption by the CCS-ORC system to capture CO_2.

Based on the results, no significant difference was observed between the values obtained from the volume and weight of the CCS-ORC system when operating with the selected sorbents. This similitude is attributed to the fact that the RWA contributes merely 6 %, on average, to the weight and volume of the CCS-ORC system.

The study further revealed that the engine's size does not drastically influence the CCS-ORC system operation since the parasitic loads provoked by the CCS-ORC system remain almost constant between engines with average values of 2.9 % at 70 % of CCR and 9 % at 100 % CCR. The CCS-ORC system exhibited similar behaviour during PPN and MOF operations. However, when operating with AC, the CCS-ORC system exhibits increased parasitic loads and energy consumption to capture the CO_2, averaging 15 % across all engine loads and rpm ranges. This increase is due to the low selectivity of AC, leading to a higher
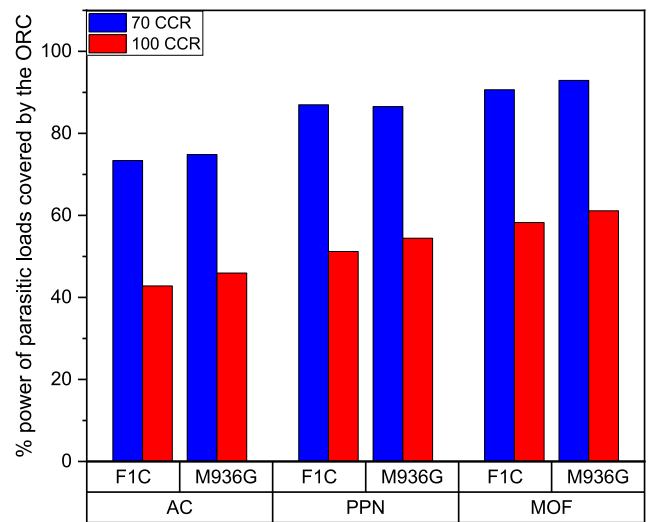
Fig. 12. Percentage of power of parasitic loads covered by the ORC.
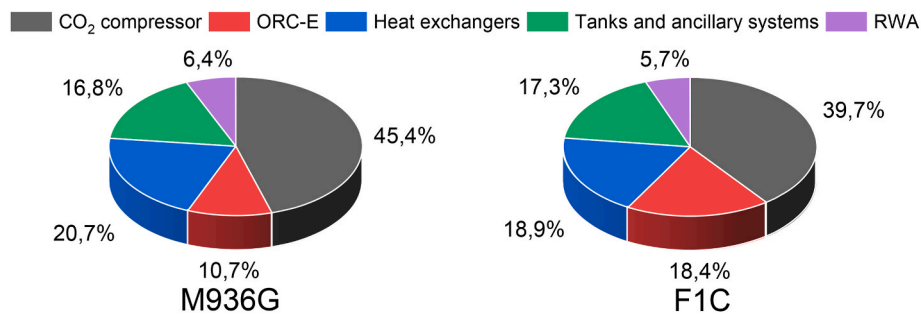
Fig. 11. Average weight of the several components of the CCS-ORS system.

Table 9
Total and percentage fuel mass increase in the engines to cover the CCS-ORC system operation at 75 % of engine load, 8 h of operation and maximum torque.

Engine	mass fuel [kg]	CCR [%]	PPN		MOF		AC	
			mass fuel [kg]	Increase mass fuel [%]	mass fuel [kg]	Increase mass fuel [%]	mass fuel [kg]	Increase mass fuel [%]
M936G	136.30	70	0.71	0.52	0.13	0.09	2.96	2.17
		100	7.04	5.17	6.09	4.47	10.22	7.5
F1C	259.54	70	1.38	0.53	0.31	0.12	4.95	1.91
		100	10.87	4.19	9.37	3.61	15.94	6.14
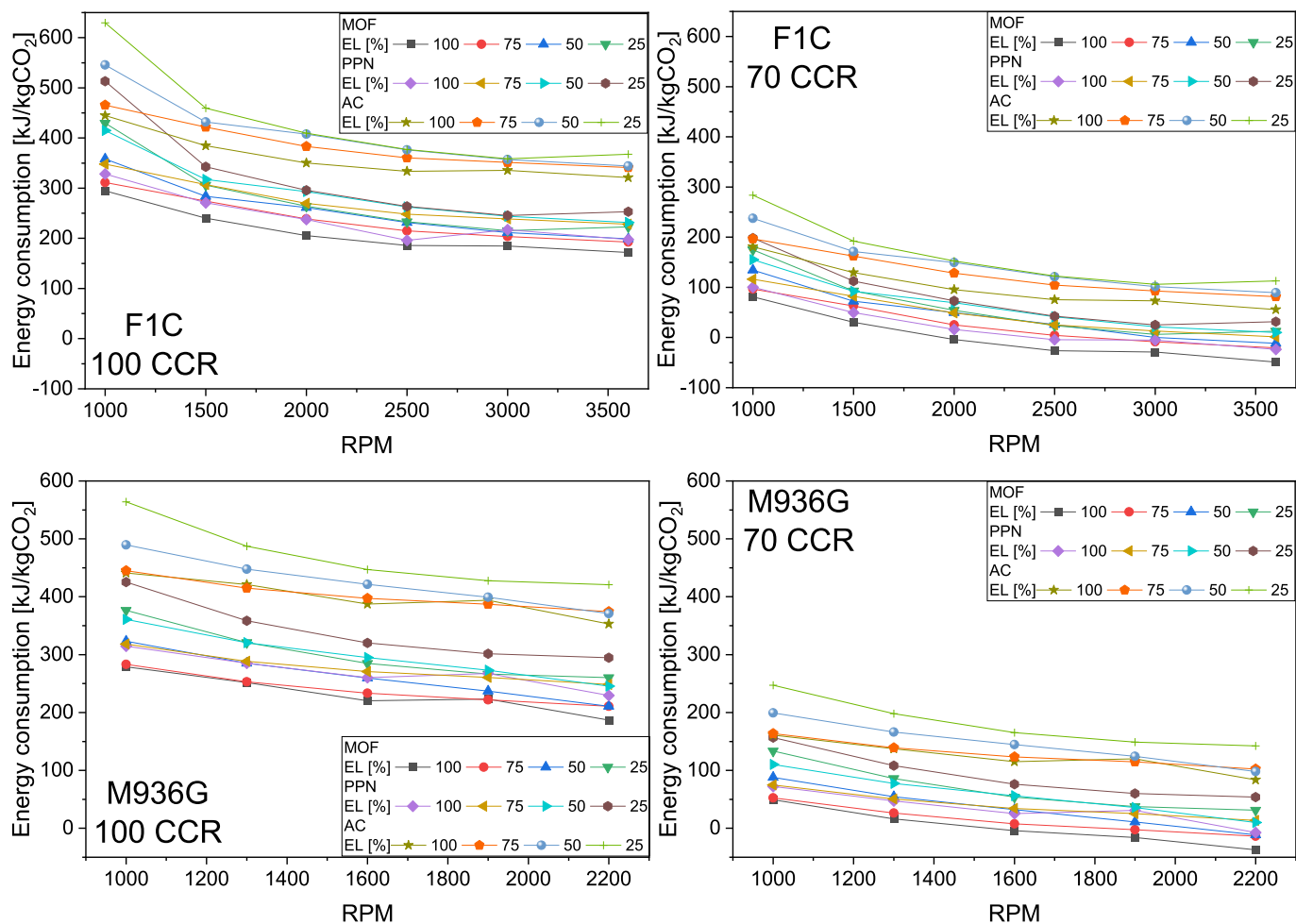
Fig. 13. Energy consumption of the CO_2 capture process.

concentration of N_2 impurities in the captured CO_2. Consequently, this necessitates greater compression power for liquefying the CO_2 and increases the energy consumption value to CO_2 capture regarding the MOF and PPN sorbents.

The information about the system's performance, weight, volume, and energy consumption obtained in this research suggests that applying this CCS-ORC technology is feasible in various sectors that utilise heavy-duty engines. Therefore, future research endeavours should focus on experimental validation of all the information provided by the simulations. Putting a particular focus on the complex operation of the RWA, the potential increase in fuel consumption of the ICE due to the additional weight of the vehicle caused by the CCS-ORC system, the sensitivity operation of the CCS-ORC system under the weather seasons and the evaluation of the adsorption and desorption times of the CO_2 of the sorbent. These areas will be the subject of further investigation by the current research team and contribute to their ongoing and future research.

CRediT authorship contribution statement

**Alexander García-Mariaca:** Conceptualization, Data curation, Formal analysis, Investigation, Methodology, Software, Writing – original draft, Writing – review & editing. **Eva Llera-Sastresa:** Conceptualization, Funding acquisition, Investigation, Methodology, Supervision, Writing – original draft, Writing – review & editing. **Francisco Moreno:** Conceptualization, Data curation, Formal analysis, Software, Supervision, Writing – review & editing.

Declaration of Competing interest

We wish to confirm no known conflicts of interest associated with this publication. There has been no significant financial support for this work that could have influenced its outcome.

We confirm that the manuscript has been read and approved by all named authors and that there are no other persons who satisfied the criteria for authorship but are not listed. We further confirm that the order of authors listed in the manuscript has been approved by all of us.

We confirm that we have given due consideration to the protection of intellectual property associated with this work and that there are no impediments to publication, including the timing of publication, concerning intellectual property. In so doing, we confirm that we have followed the regulations of our institutions concerning intellectual property.

We understand that the Corresponding Author is the sole contact for the Editorial process (including Editorial Manager and direct communications with the office). He is responsible for communicating with the other authors about progress, submissions of revisions and final approval of proofs. We confirm that we have provided a current, correct email address accessible by the Corresponding Author.

Data availability

Data will be made available on request.

Appendix A. Temperature, pressure, mass flow, and composition of the exhaust gases (Input parameters in the CCS-ORC simulations) obtained with the M936G engine model

Load	rpm	T_{EG} [°C]	$\dot{m}_{EG}$ [kg/s]	$\dot{m}_{CO2}$ [kg/s]	$\dot{m}_{H2O}$ [kg/s]	$\dot{m}_{N2}$ [kg/s]	Pressure [bar]
100	1000	565.45	0.1084	0.01670	0.01370	0.07800	1.09
100	1300	595.00	0.1470	0.02270	0.01860	0.10570	
100	1600	622.35	0.18925	0.02920	0.02390	0.13610	
100	1900	637.75	0.2096	0.03240	0.02650	0.15080	
100	2200	663.15	0.1969	0.03040	0.02490	0.14170	
75	1000	559.65	0.09203	0.01420	0.01160	0.06626	1.09
75	1300	588.9	0.13321	0.02050	0.01679	0.09590	
75	1600	607.75	0.16007	0.02470	0.02017	0.11524	
75	1900	618.65	0.17691	0.02725	0.02230	0.12736	
75	2200	626.75	0.16704	0.02573	0.02105	0.12026	
50	1000	523.65	0.07441	0.01138	0.00931	0.05373	1.09
50	1300	556.5	0.10554	0.01614	0.01320	0.07621	
50	1600	579.85	0.12860	0.01966	0.01609	0.09285	
50	1900	599.95	0.14275	0.02182	0.01786	0.10307	
50	2200	620.95	0.13467	0.02059	0.01684	0.09724	
25	1000	481.25	0.05788	0.00880	0.00720	0.04187	1.09
25	1300	524.00	0.08212	0.01249	0.01022	0.05941	
25	1600	554.35	0.10012	0.01523	0.01246	0.07244	
25	1900	570.35	0.11068	0.01683	0.01377	0.08007	
25	2200	574.95	0.10445	0.01589	0.01300	0.07557	

Appendix B. Temperature, pressure, mass flow, and composition of the exhaust gases (Input parameters in the CCS-ORC simulations) obtained with the F1C engine model

Load	rpm	T_{EG} [°C]	$\dot{m}_{EG}$ [kg/s]	$\dot{m}_{CO2}$ [kg/s]	$\dot{m}_{H2O}$ [kg/s]	$\dot{m}_{N2}$ [kg/s]	Pressure [bar]
100	1000	523.15	0.03464	0.00534	0.00437	0.02493	1.09
100	1500	575.00	0.05806	0.00897	0.00734	0.04176	
100	2000	610.00	0.07688	0.01187	0.00971	0.05529	
100	2500	630.50	0.09893	0.01528	0.01250	0.07115	
100	3000	656.95	0.11314	0.01746	0.01429	0.08139	
100	3600	673.95	0.11258	0.01742	0.01425	0.08092	
75	1000	505.95	0.02922	0.00450	0.00368	0.02103	1.09
75	1500	540.00	0.04900	0.00755	0.00617	0.03528	
75	2000	580.00	0.06489	0.01000	0.00818	0.04671	
75	2500	600.00	0.08395	0.01296	0.01060	0.06039	
75	3000	611.85	0.09609	0.01476	0.01208	0.06926	
75	3600	621.45	0.09709	0.01477	0.01208	0.07024	
50	1000	467.95	0.02373	0.00361	0.00295	0.01716	1.09
50	1500	528.00	0.03900	0.00602	0.00495	0.02860	
50	2000	550.50	0.05250	0.00800	0.00660	0.03800	
50	2500	575.00	0.06750	0.01030	0.00845	0.04880	
50	3000	599.70	0.07775	0.01185	0.00970	0.05620	
50	3600	610.75	0.07720	0.01179	0.00965	0.05577	
25	1000	428.55	0.01859	0.00280	0.00229	0.01349	1.09
25	1500	504.00	0.03070	0.00470	0.00385	0.02250	
25	2000	542.00	0.04100	0.00625	0.00513	0.02980	
25	2500	572.00	0.05300	0.00800	0.00660	0.03860	
25	3000	589.65	0.06073	0.00915	0.00749	0.04409	
25	3600	582.95	0.06113	0.00914	0.00748	0.04451	

Appendix C. Adsorption and desorption heat at 100 % of CCR in the M936G engine

Load	rpm	PPN		MOF		AC	
		Q_{ads} [kW]	Q_{des} [kW]	Q_{ads} [kW]	Q_{des} [kW]	Q_{ads} [kW]	Q_{des} [kW]
100	1000	−27.3251	25.6312	−22.3638	20.6699	−27.3466	25.6527
100	1300	−37.0679	34.7701	−30.3376	28.0398	−37.0971	34.7992
100	1600	−47.7225	44.7642	−39.0577	36.0994	−47.7600	44.8017
100	1900	−52.8597	49.5829	−43.2622	39.9854	−52.9013	49.6245

(continued)

Load	rpm	PPN		MOF		AC	
		Q_{ads} [kW]	Q_{des} [kW]	Q_{ads} [kW]	Q_{des} [kW]	Q_{ads} [kW]	Q_{des} [kW]
100	2200	−49.6584	46.5800	−40.6421	37.5638	−49.6974	46.6191
75	1000	−23.1591	21.7234	−18.9542	17.5185	−23.1773	21.7416
75	1300	−33.5220	31.4439	−27.4355	25.3575	−33.5483	31.4703
75	1600	−40.2806	37.7836	−32.9671	30.4701	−40.3123	37.8153
75	1900	−44.5168	41.7572	−36.4341	33.6745	−44.5519	41.7923
75	2200	−42.0343	39.4286	−34.4023	31.7966	−42.0673	39.4616
50	1000	−18.5845	17.4324	−15.2102	14.0581	−18.5991	17.4471
50	1300	−26.3587	24.7248	−21.5729	19.9389	−26.3795	24.7455
50	1600	−32.1167	30.1258	−26.2854	24.2945	−32.1420	30.1511
50	1900	−35.6516	33.4416	−29.1785	26.9685	−35.6797	33.4696
50	2200	−33.6330	31.5481	−27.5264	25.4415	−33.6594	31.5745
25	1000	−14.3795	13.4881	−11.7686	10.8773	−14.3908	13.4994
25	1300	−20.4039	19.1391	−16.6993	15.4344	−20.4200	19.1551
25	1600	−24.8755	23.3335	−20.3590	18.8170	−24.8951	23.3531
25	1900	−27.4984	25.7938	−22.5056	20.8010	−27.5200	25.8154
25	2200	−25.9518	24.3431	−21.2399	19.6311	−25.9722	24.3635

Appendix D. Adsorption and desorption heat at 70 % of CCR in the M936G engine

Load	rpm	PPN		MOF		AC	
		Q_{ads} [kW]	Q_{des} [kW]	Q_{ads} [kW]	Q_{ads} [kW]	Q_{des} [kW]	Q_{ads} [kW]
100	1000	−19.1276	17.9418	−15.6546	14.4689	−19.1426	17.9569
100	1300	−25.9475	24.3390	−21.2363	19.6279	−25.9679	24.3595
100	1600	−33.4057	31.3349	−27.3404	25.2696	−33.4320	31.3612
100	1900	−37.0018	34.7081	−30.2835	27.9898	−37.0309	34.7372
100	2200	−34.7608	32.6060	−28.4495	26.2946	−34.7882	32.6334
75	1000	−16.2113	15.2064	−13.2679	12.2630	−16.2241	15.2192
75	1300	−23.4654	22.0108	−19.2049	17.7502	−23.4838	22.0292
75	1600	−28.1964	26.4486	−23.0769	21.3290	−28.2186	26.4707
75	1900	−31.1618	29.2301	−25.5039	23.5722	−31.1863	29.2546
75	2200	−29.4240	27.6000	−24.0816	22.2576	−29.4471	27.6231
50	1000	−13.0091	12.2027	−10.6471	9.8407	−13.0194	12.2129
50	1300	−18.4511	17.3073	−15.1010	13.9572	−18.4656	17.3218
50	1600	−22.4817	21.0881	−18.3998	17.0062	−22.4994	21.1058
50	1900	−24.9561	23.4091	−20.4250	18.8779	−24.9758	23.4287
50	2200	−23.5431	22.0837	−19.2685	17.8090	−23.5616	22.1022
25	1000	−10.0656	9.4417	−8.2381	7.6141	−10.0735	9.4496
25	1300	−14.2828	13.3974	−11.6895	10.8041	−14.2940	13.4086
25	1600	−17.4129	16.3335	−14.2513	13.1719	−17.4266	16.3472
25	1900	−19.2489	18.0557	−15.7540	14.5607	−19.2640	18.0708
25	2200	−18.1663	17.0402	−14.8679	13.7418	−18.1806	17.0544

Appendix E. Adsorption and desorption heat at 100 % of CCR in the F1C engine

Load	rpm	PPN		MOF		AC	
		Q_{ads} [kW]	Q_{des} [kW]	Q_{ads} [kW]	Q_{ads} [kW]	Q_{des} [kW]	Q_{ads} [kW]
100	1000	−8.7208	8.1802	−7.1374	6.5968	−8.7277	8.1871
100	1500	−14.6488	13.7407	−11.9891	11.0810	−14.6603	13.7522
100	2000	−19.3949	18.1926	−15.8734	14.6711	−19.4101	18.2078
100	2500	−24.9579	23.4107	−20.4264	18.8792	−24.9775	23.4304
100	3000	−28.5223	26.7542	−23.3437	21.5756	−28.5448	26.7767
100	3600	−28.4511	26.6874	−23.2854	21.5217	−28.4735	26.7098
75	1000	−7.3543	6.8984	−6.0190	5.5631	−7.3601	6.9042
75	1500	−12.3270	11.5628	−10.0888	9.3247	−12.3367	11.5725
75	2000	−16.3365	15.3238	−13.3703	12.3576	−16.3493	15.3366
75	2500	−21.1665	19.8544	−17.3234	16.0113	−21.1831	19.8710
75	3000	−24.1111	22.6165	−19.7334	18.2387	−24.1301	22.6354
75	3600	−24.1294	22.6336	−19.7483	18.2525	−24.1484	22.6526
50	1000	−5.8999	5.5341	−4.8287	4.4629	−5.9045	5.5388
50	1500	−9.8344	9.2248	−8.0488	7.4392	−9.8421	9.2325
50	2000	−13.0690	12.2588	−10.6961	9.8859	−13.0792	12.2691
50	2500	−16.8263	15.7832	−13.7712	12.7281	−16.8395	15.7965
50	3000	−19.3605	18.1603	−15.8453	14.6451	−19.3757	18.1756
50	3600	−19.2598	18.0659	−15.7629	14.5690	−19.2750	18.0811
25	1000	−4.5741	4.2906	−3.7436	3.4601	−4.5777	4.2942
25	1500	−7.6780	7.2021	−6.2839	5.8080	−7.6841	7.2081

(*continued*)

Load	rpm	PPN		MOF		AC	
		Q_{ads} [kW]	Q_{des} [kW]	Q_{ads} [kW]	Q_{ads} [kW]	Q_{des} [kW]	Q_{ads} [kW]
25	2000	−10.2101	9.5772	−8.3563	7.7234	−10.2182	9.5852
25	2500	−13.0690	12.2588	−10.6961	9.8859	−13.0792	12.2691
25	3000	−14.9470	14.0204	−12.2331	11.3066	−14.9588	14.0322
25	3600	−14.9340	14.0083	−12.2225	11.2968	−14.9458	14.0200

Appendix F. Adsorption and desorption heat at 70 % of CCR in the F1C engine

Load	rpm	PPN		MOF		AC	
		Q_{ads} [kW]	Q_{des} [kW]	Q_{ads} [kW]	Q_{ads} [kW]	Q_{des} [kW]	Q_{ads} [kW]
100	1000	−6.1046	5.7262	−4.9962	4.6178	−6.1094	5.7310
100	1500	−10.2541	9.6185	−8.3923	7.7567	−10.2622	9.6265
100	2000	−13.5764	12.7348	−11.1114	10.2698	−13.5871	12.7455
100	2500	−17.4705	16.3875	−14.2985	13.2155	−17.4843	16.4013
100	3000	−19.9656	18.7280	−16.3406	15.1029	−19.9813	18.7437
100	3600	−19.9158	18.6812	−16.2997	15.0652	−19.9314	18.6969
75	1000	−5.1480	4.8289	−4.2133	3.8942	−5.1521	4.8329
75	1500	−8.6289	8.0940	−7.0622	6.5273	−8.6357	8.1008
75	2000	−11.4355	10.7267	−9.3592	8.6504	−11.4445	10.7356
75	2500	−14.8165	13.8981	−12.1264	11.2079	−14.8282	13.9097
75	3000	−16.8778	15.8315	−13.8134	12.7671	−16.8911	15.8448
75	3600	−16.8906	15.8435	−13.8238	12.7768	−16.9038	15.8568
50	1000	−4.1299	3.8739	−3.3801	3.1240	−4.1332	3.8771
50	1500	−6.8841	6.4573	−5.6342	5.2074	−6.8895	6.4627
50	2000	−9.1483	8.5812	−7.4873	6.9202	−9.1555	8.5884
50	2500	−11.7784	11.0483	−9.6398	8.9097	−11.7877	11.0575
50	3000	−13.5523	12.7122	−11.0917	10.2516	−13.5630	12.7229
50	3600	−13.4819	12.6461	−11.0340	10.1983	−13.4925	12.6567
25	1000	−3.2019	3.0034	−2.6205	2.4220	−3.2044	3.0059
25	1500	−5.3746	5.0414	−4.3988	4.0656	−5.3788	5.0457
25	2000	−7.1471	6.7040	−5.8494	5.4064	−7.1527	6.7097
25	2500	−9.1483	8.5812	−7.4873	6.9202	−9.1555	8.5884
25	3000	−10.4629	9.8143	−8.5632	7.9146	−10.4711	9.8225
25	3600	−10.4538	9.8058	−8.5558	7.9077	−10.4621	9.8140

Appendix G. Thermal and combustion efficiencies in the M936G engine

Load	rpm	η_{th} [%]	η_{com} [%]
100	1000	38.81	98.53
100	1300	41.14	98.55
100	1600	39.82	98.54
100	1900	38.04	98.56
100	2200	35.35	98.58
75	1000	31.72	98.58
75	1300	34.16	98.58
75	1600	33.39	98.59
75	1900	31.76	98.59
75	2200	28.91	98.62
50	1000	22.25	98.66
50	1300	25.88	98.62
50	1600	25.09	98.62
50	1900	23.57	98.64
50	2200	20.87	98.63
25	1000	10.58	98.75
25	1300	12.18	98.71
25	1600	12.00	98.70
25	1900	10.95	98.70
25	2200	8.83	98.73

Appendix H. Thermal and combustion efficiencies in the F1C engine

Load	rpm	η_{th} [%]	η_{com} [%]
100	1000	32.58	97.83
100	1500	34.50	97.82
100	2000	35.01	97.82
100	2500	33.60	97.86
100	3000	30.86	97.84
100	3600	27.35	97.88
75	1000	27.85	97.87
75	1500	29.10	97.84
75	2000	29.44	97.84
75	2500	27.80	97.90
75	3000	25.17	97.92
75	3600	20.36	98.01
50	1000	20.26	98.01
50	1500	22.10	97.98
50	2000	22.58	97.94
50	2500	21.05	97.94
50	3000	18.47	98.00
50	3600	15.56	98.04
25	1000	8.80	98.28
25	1500	10.24	98.18
25	2000	10.61	98.14
25	2500	10.12	98.12
25	3000	8.75	98.14
25	3600	5.67	98.25

References

[1] Li Z, Khajepour A, Song J. A comprehensive review of the key technologies for pure electric vehicles. Energy 2019;182:824–39. https://doi.org/10.1016/j.energy.2019.06.077.

[2] Li S, Djilali N, Rosen MA, Crawford C, Sui PC. Transition of heavy-duty trucks from diesel to hydrogen fuel cells: Opportunities, challenges, and recommendations. Int J Energy Res 2022;46:11718–29. https://doi.org/10.1002/er.8066.

[3] Biresselioglu ME, Demirbag Kaplan M, Yilmaz BK. Electric mobility in Europe: a comprehensive review of motivators and barriers in decision making processes. Transp Res Part A Policy Pract 2018;109:1–13. https://doi.org/10.1016/j.tra.2018.01.017.

[4] Rose L, Hussain M, Ahmed S, Malek K, Costanzo R, Kjeang E. A comparative life cycle assessment of diesel and compressed natural gas powered refuse collection vehicles in a Canadian city. Energy Pol 2013;52:453–61. https://doi.org/10.1016/j.enpol.2012.09.064.

[5] Quiros DC, Smith J, Thiruvengadam A, Huai T, Hu S. Greenhouse gas emissions from heavy-duty natural gas, hybrid, and conventional diesel on-road trucks during freight transport. Atmos Environ 2017;168:36–45. https://doi.org/10.1016/j.atmosenv.2017.08.066.

[6] European Commission. Amending Delegated Regulation (EU) 2021/2139 as regards economic activities in certain energy sectors and Delegated Regulation (EU) 2021/2178 as regards specific public disclosures for those economic activities. 2022. Brussels.

[7] Pasini G, Lutzemberger G, Ferrari L. Renewable Electricity for Decarbonisation of road transport: Batteries or E-fuels? Batteries 2023;9. https://doi.org/10.3390/batteries9020135.

[8] Budinis S, Krevor S, Dowell N Mac, Brandon N, Hawkes A. An assessment of CCS costs, barriers and potential. Energy Strategy Rev 2018;22:61–81. https://doi.org/10.1016/j.esr.2018.08.003.

[9] Feenstra M, Monteiro J, van den Akker JT, Abu-Zahra MRM, Gilling E, Goetheer E. Ship-based carbon capture onboard of diesel or LNG-fuelled ships. Int J Greenh Gas Control 2019;85:1–10. https://doi.org/10.1016/j.ijggc.2019.03.008.

[10] Ozaki M, Nakazawa N, Omata A, Komatsu M, Manabe H. Ship-Based carbon dioxide capture and storage for enhanced oil recovery. Proceedings of the Annual Offshore Technology Conference 2015;4:2412–25. https://doi.org/10.4043/25861-ms.

[11] Ros JA, Skylogianni E, Doedée V, van den Akker JT, Vredeveldt AW, Linders MJG, et al. Advancements in ship-based carbon capture technology on board of LNG-fuelled ships. Int J Greenh Gas Control 2022;114:103575. https://doi.org/10.1016/J.IJGGC.2021.103575.

[12] Francisco ARL. Ship-based transport of CO₂. J Chem Inf Model 2013;53:1689–99. https://doi.org/10.1017/CBO9781107415324.004.

[13] Saravanan S, Kumar R. Experimental investigations on CO₂ recovery from engine exhaust using adsorption technology. SAE Technical Paper 2019. https://doi.org/10.4271/2019-28-2577.Abstract. 2019-28-2577.

[14] Kumar P, Rathod V, Parwani AK. Experimental investigation on performance of absorbents for carbon dioxide capture from diesel engine exhaust. Environ Prog Sustain Energy 2021;40. https://doi.org/10.1002/ep.13651.

[15] Rajdurai MS, Rao AHS, Kamalakkannan K. CO₂ capture using activated Alumina in gasoline passenger vehicles. Int J Eng Res Appl 2016;6:73–7.

[16] García-Mariaca A, Llera-Sastresa E. Energy and economic analysis feasibility of CO₂ capture on a natural gas internal combustion engine. Greenhouse Gases: Sci Technol 2022. https://doi.org/10.1002/GHG.2176.

[17] Awoyomi A, Patchigolla K, Anthony EJ. Process and economic evaluation of an onboard capture system for LNG-Fueled CO₂ carriers. Ind Eng Chem Res 2020;59: 6951–60. https://doi.org/10.1021/acs.iecr.9b04659.

[18] Horvath S, Fasihi M, Breyer C. Techno-economic analysis of a decarbonized shipping sector: technology suggestions for a fleet in 2030 and 2040. Energy Convers Manag 2018;164:230–41. https://doi.org/10.1016/j.enconman.2018.02.098.

[19] Fang S, Xu Y, Li Z, Ding Z, Liu L, Wang H. Optimal sizing of shipboard carbon capture system for maritime greenhouse emission control. IEEE Trans Ind Appl 2019;55. https://doi.org/10.1109/tia.2019.2934088. 1–1.

[20] Aramco. Capturing carbon on the move. 2019. https://www.aramco.com/en/creating-value/technology-development/transport-tech nologies/mobile-carbon-capture#. [Accessed 19 February 2023].

[21] Al-Meshari AA, Muhaish FI, Aleidan AA. Carbon capture: Saudi aramco's carbon management program. J Petrol Technol 2014;66:72–4. https://doi.org/10.2118/0614-0072-jpt.

[22] Voice A, Hamad E. Mobile carbon capture for long-haul commercial transport: design, integration and results. SSRN Electron J 2022. https://doi.org/10.2139/ssrn.4280720.

[23] Omata A, Hattori K. Preliminary feasibility study on CO₂ carrier for ship-based CCS. Global CCS Institute; 2011. p. 1–180.

[24] Larkin C, Lampri K, Mazzone S, Oliva F, Li K, García-García FR. Retrofitting hollow fibre carbon capture systems to decarbonise surface transport. J CO2 Util 2023;67. https://doi.org/10.1016/j.jcou.2022.102336.

[25] Sharma S, Maréchal F. Carbon dioxide capture from internal combustion engine exhaust using temperature swing adsorption. Front Energy Res 2019;7:1–12. https://doi.org/10.3389/fenrg.2019.00143.

[26] García-Mariaca A, Llera-Sastresa E. Review on carbon capture in ICE driven transport. Energies 2021;14:6865. https://doi.org/10.3390/en14216865.

[27] García-Mariaca A, Llera-Sastresa E, Moreno F. Application of ORC to reduce the energy penalty of carbon capture in non-stationary ICE. Energy Convers Manag 2022;268:116029. https://doi.org/10.1016/J.ENCONMAN.2022.116029.

[28] Hoffmann Kai, Benz Michael, Marko Weirich. The new mercedes-benz medium duty commercial natural gas engine. MTZ Worldw 2014;75:4–11. https://doi.org/10.1007/s38313-014-0251-4.

[29] Iveco company. IVECO DAILY technical information. 2015. p. 1–39. https://www.iveco.com/Denmark/Documents/Configurator/Brochure/Dailyvan_DK.pdf. [Accessed 8 February 2023].

[30] Mercedes-Benz. Citaro NGT technical information 2017:16. https://www.mercede s-benz-bus.com/content/dam/mbo/markets/common/buy/services-online/downl oad-technical-brochures/images/content/regular-service-buses/citaro-ngt/MB-NGT-2-ES-09_17.pdf (accessed March 8, 2023)..

[31] Iveco company. IVECO change your business perspective 2021;1-44. https://viewe r.ipaper.io/iveco-hq/uk/Daily-Van/?page=6 (accessed April 22, 2023)..

[32] Obiols J, Soleri D, Dioc N, Moreau M. Potential of concomitant injection of CNG and gasoline on a 1.6L gasoline direct injection turbocharged engine. SAE Technical Papers 2011. https://doi.org/10.4271/2011-01-1995.

[33] Yontar AA, Doğu Y. Effects of equivalence ratio and CNG addition on engine performance and emissions in a dual sequential ignition engine. Int J Engine Res 2020;21:1067–82. https://doi.org/10.1177/1468087419834190.

[34] López JJ, Novella R, Gomez-Soriano J, Martinez-Hernandiz PJ, Rampanarivo F, Libert C, et al. Advantages of the unscavenged pre-chamber ignition system in turbocharged natural gas engines for automotive applications. Energy 2021;218: 119466. https://doi.org/10.1016/j.energy.2020.119466.

[35] Hovington P, Ghaffari-Nik O, Mariac L, Liu A, Henkel B, Marx S. Rapid cycle temperature swing adsorption process using solid structured sorbent for CO_2 capture from cement flue gas. SSRN Electron J 2021. https://doi.org/10.2139/ssrn.3814414.

[36] Peris B, Navarro-Esbrí J, Molés F. Bottoming organic Rankine cycle configurations to increase Internal Combustion Engines power output from cooling water waste heat recovery. Appl Therm Eng 2013;61:364–71. https://doi.org/10.1016/j.applthermaleng.2013.08.016.

[37] Invernizzi CM, Iora P, Manzolini G, Lasala S. Thermal stability of n-pentane, cyclo-pentane and toluene as working fluids in organic Rankine engines. Appl Therm Eng 2017;121:172–9. https://doi.org/10.1016/j.applthermaleng.2017.04.038.

[38] Shu G, Li X, Tian H, Liang X, Wei H, Wang X. Alkanes as working fluids for high-temperature exhaust heat recovery of diesel engine using organic Rankine cycle. Appl Energy 2014;119:204–17. https://doi.org/10.1016/j.apenergy.2013.12.056.

[39] Scaccabarozzi R, Tavano M, Invernizzi CM. Comparison of working fluids and cycle optimization for heat recovery ORCs from large internal combustion engines. Energy 2018. https://doi.org/10.1016/j.energy.2018.06.017.

[40] Invernizzi CM, Bonalumi D. Thermal stability of organic fluids for Organic Rankine Cycle systems. In: Organic Rankine cycle (ORC) power systems. Woodhead Publishing; 2017. p. 121–51. https://doi.org/10.1016/B978-0-08-100510-1.00005-3.

[41] Fatigati F, di Battista D, Cipollone R. Permeability effects assessment on recovery performances of small-scale ORC plant. Appl Therm Eng 2021;196:117331. https://doi.org/10.1016/J.APPLTHERMALENG.2021.117331.

[42] Fatigati F, Di Bartolomeo M, Di Battista D, Cipollone R. Experimental and numerical characterization of the sliding rotary vane expander intake pressure in order to develop a novel control-diagnostic procedure. Energies 2019;12:1970. https://doi.org/10.3390/en12101970.

[43] Fatigati F, di Bartolomeo M, di Battista D, Cipollone R. Experimental characterization of a hermetic scroll expander operating in an ORC-based power unit bottoming an internal combustion engine. In: AIP conf proc. American Institute of Physics Inc; 2019. https://doi.org/10.1063/1.5138802. 2191.

[44] Kind Matthias, Martin Holger. VDI heat atlas. Second. Berlin: Springer; 2010. https://doi.org/10.1007/978-3-540-77877-6.

[45] Yakah Noah. Heat exchanger design for a solar gas-turbine power plant. Master of science Thesis. KTH School of Industrial Engineering and Management; 2012.

[46] Ping X, Yang F, Zhang H, Zhang J, Zhang W, Song G. Introducing machine learning and hybrid algorithm for prediction and optimization of multistage centrifugal pump in an ORC system. Energy 2021;222. https://doi.org/10.1016/j.energy.2021.120007.

[47] Vodicka V, Novotny V, Mascuch J, Kolovratnik M. Impact of major leakages on characteristics of a rotary vane expander for ORC. Energy Proc 2017;129:387–94. https://doi.org/10.1016/j.egypro.2017.09.249. Elsevier Ltd.

[48] Perry RH, Green DW, Maloney JO. Perry's chemical engineers' handbook. McGraw-Hill; 1997.

[49] Gibson JAA, Mangano E, Shiko E, Greenaway AG, Gromov AV, Lozinska MM, et al. Adsorption materials and processes for carbon capture from gas-Fired power plants: AMPGas. Ind Eng Chem Res 2016;55:3840–51. https://doi.org/10.1021/acs.iecr.5b05015.

[50] Huck JM, Lin LC, Berger AH, Shahrak MN, Martin RL, Bhown AS, et al. Supporting Information: Evaluating different classes of porous materials for carbon capture. Energy Environ Sci 2014;7:4132–46. https://doi.org/10.1039/c4ee02636e.

[51] Verdegaal WM, Wang K, Sculley JP, Wriedt M, Zhou HC. Evaluation of metal-organic frameworks and porous Polymer Networks for CO_2-capture applications. ChemSusChem 2016;9:636–43. https://doi.org/10.1002/cssc.201501464.

[52] Lu C, Bai H, Wu B, Su F, Hwang JF. Comparative study of CO_2 capture by carbon nanotubes, activated carbons, and zeolites. Energy Fuel 2008;22:3050–6. https://doi.org/10.1021/ef8000086.

[53] Himeno S, Komatsu T, Fujita S. High-pressure adsorption equilibria of methane and carbon dioxide on several activated carbons. J Chem Eng Data 2005;50:369–76. https://doi.org/10.1021/je049786x.

[54] Plaza MG, García S, Rubiera F, Pis JJ, Pevida C. Post-combustion CO_2 capture with a commercial activated carbon: comparison of different regeneration strategies. Chem Eng J 2010;163:41–7. https://doi.org/10.1016/j.cej.2010.07.030.

[55] You YY, Liu XJ. Modeling of CO_2 adsorption and recovery from wet flue gas by using activated carbon. Chem Eng J 2019;369:672–85. https://doi.org/10.1016/j.cej.2019.03.118.

[56] Emerson Climate Technologies. Copeland TM Stream Semi-Hermetic Compressors for Use with CO_2 in Transcritical & Subcritical Application Application Guidelines. 2019. p. 1–47. https://www.copeland.com/documents/copeland-stream-co2-semi-hermetic-compressors-for-use-co2-in-transcritical-subcritical-applications-4mtl-05-to-4mtl-50-4msl-03-to-4msl-15-application-guidelines-en-gb-4218052.pdf. [Accessed 29 December 2023].

[57] Yang K, Zhang H, Song S, Zhang J, Wu Y, Zhang Y, et al. Performance analysis of the vehicle diesel engine-ORC combined system based on a screw expander. Energies 2014;7:3400–19. https://doi.org/10.3390/en7053400.

[58] Zhang YQ, Wu YT, Xia GD, Ma CF, Ji WN, Liu SW, et al. Development and experimental study on organic Rankine cycle system with single-screw expander for waste heat recovery from exhaust of diesel engine. Energy 2014;77:499–508. https://doi.org/10.1016/J.ENERGY.2014.09.034.

[59] Pezzella G, Bhatt PM, AlHaji A, Ramirez A, Grande CA, Gascon J, et al. Onboard capture and storage system using metal-organic frameworks for reduced carbon dioxide emissions from vehicles. Cell Rep Phys Sci 2023;4:101467. https://doi.org/10.1016/j.xcrp.2023.101467.

[60] Casadei A, Broda R, Ricardo Inc. Impact of vehicle weight reduction on fuel economy for various vehicle architectures. The Aluminum Association, Inc; 2008. p. 1–60. copy obtained from, https://www.h3xed.com/blogmedia/Ricardo_FE_MPG_Study.pdf. [Accessed 7 January 2024].

[61] Shu G, Zhao M, Tian H, Wei H, Liang X, Huo Y, et al. Experimental investigation on thermal OS/ORC (Oil Storage/Organic Rankine Cycle) system for waste heat recovery from diesel engine. Energy 2016;107:693–706. https://doi.org/10.1016/J.ENERGY.2016.04.062.

[62] Lin S, Zhao L, Deng S, Ni J, Zhang Y, Ma M. Dynamic performance investigation for two types of ORC system driven by waste heat of automotive internal combustion engine. Energy 2019;169:958–71. https://doi.org/10.1016/j.energy.2018.12.092.

[63] Kim J, Yoo Y, Kim S, Beak J, Oh S-D, Lee J, et al. Design and assessment of a novel mobile carbon capture system: energy and exergy analyses. Energy Convers Manag 2024;300:117934. https://doi.org/10.1016/j.enconman.2023.117934.

[64] Jiang N, Shen Y, Liu B, Zhang D, Tang Z, Li G, et al. CO_2 capture from dry flue gas by means of VPSA, TSA and TVSA. J CO2 Util 2020;35:153–68. https://doi.org/10.1016/j.jcou.2019.09.012.

[65] Wu K, Deng S, Li S, Zhao R, Yuan X, Zhao L. Preliminary experimental study on the performance of CO_2 capture prototype based on temperature swing adsorption (TSA). Carbon Capture Science and Technology 2022;2. https://doi.org/10.1016/j.ccst.2022.100035.

[66] Li H, Guo H, Shen S. Low-energy-consumption CO_2 capture by liquid-solid phase change absorption using water-lean blends of amino acid salts and 2-alkoxyethanols. ACS Sustain Chem Eng 2020;8:12956–67. https://doi.org/10.1021/acssuschemeng.0c03525.

[67] Tian W, Ma K, Ji J, Tang S, Zhong S, Liu C, et al. Nonaqueous MEA/PEG200 absorbent with high efficiency and low energy consumption for CO_2 capture. Ind Eng Chem Res 2021;60:3871–80. https://doi.org/10.1021/acs.iecr.0c05294.